Ocean-Bottom Seismometer Deployment on the Laurentian Fan Seismic Zone: The First Long-Term Test for the Canadian National Facility for Seismological Investigations

Elahe Sirati[*1], Alexandre P. Plourde[1,2], Mladen R. Nedimović[1], Miao Zhang[1], Graeme Cairns[1], Katie Bosman[1], John Thibodeau[1], Alireza Niksejel[1], Pascal Audet[3], Michael G. Bostock[4], Andrew J. Calvert[5], Fiona A. Darbyshire[6], Stan E. Dosso[7], Andrew W. Frederiksen[8], Qinya Liu[9], Yajing Liu[10], Andrew J. Schaeffer[11], and J. Kim Welford[12]

Abstract

In November 2021, the Canadian National Facility for Seismological Investigations launched its first long-term test of the new Güralp Aquarius broadband ocean-bottom seismometers (OBS). The study targeted the lower Laurentian Fan seismic zone (~4.5 km water depth), a seismically active zone of oceanic lithosphere downslope from the epicenter of the 1929 Grand Banks earthquake (M_s 7.2) offshore Atlantic Canada. A total of 12 OBS were deployed, of which eight were recovered during an August 2022 recovery cruise, with three months of data suitable for analysis. Because of the absence of Global Positioning System clock synchronization, we performed ambient noise cross-correlation to assess clock drift; seven OBS displayed negligible drift, but one OBS clock had a relative drift of 1.14 s over the three months and was corrected before further analyses. We estimated the orientations of horizontal OBS components using particle-motion analysis of *P* waves from four teleseismic earthquakes ($M_w \geq 6.8$) and their tilt angles using a noise-based transfer-function technique. We then scanned the data for local-to-regional earthquakes using machine learning-based phase picking and automated association tools. Seventeen earthquakes were identified, including two detected by Earthquakes Canada, with estimated local magnitudes up to 2.2 and depths reaching ~39 km relative to the seafloor. Seismic data also revealed baleen whale calls in the 15–25 Hz range. Using the double-spectrogram method, we detected fin and blue whale vocalizations. Applying a hybrid double-pair double-difference method with cross-correlation delay times, we provide one example 24-hr blue whale track, spanning ~58 km.

Cite this article as Sirati, E., A. P. Plourde, M. R. Nedimović, M. Zhang, G. Cairns, K. Bosman, J. Thibodeau, A. Niksejel, P. Audet, M. G. Bostock, *et al.* (2026). Ocean-Bottom Seismometer Deployment on the Laurentian Fan Seismic Zone: The First Long-Term Test for the Canadian National Facility for Seismological Investigations, *Seismol. Res. Lett.* **XX**, 1–21, doi: 10.1785/0220260156.

Supplemental Material

Introduction

Compared with terrestrial seismometers, ocean-bottom seismometers (OBS) have a relatively short history as tools for recording natural seismicity. Autonomous OBS were first deployed to monitor local earthquakes in the 1980s, but only for periods of up to a few weeks (Ewing and Meyer, 1982; Toomey *et al.*, 1988). These deployments used short-period OBS, with typical natural frequencies of approximately 1 to 5 Hz, which were more commonly used for controlled-source surveys (Kasahara *et al.*, 1980). In the mid-1990s, OBS capable

1. Department of Earth and Environmental Sciences, Dalhousie University, Halifax, Canada, https://orcid.org/0009-0005-9794-479X (ES); https://orcid.org/0000-0001-8519-9271 (APP); https://orcid.org/0000-0003-0327-5192 (MRN); https://orcid.org/0000-0002-2555-7134 (MZ); https://orcid.org/0009-0003-8380-2198 (GC); 2. Geological Survey of Canada Atlantic, Natural Resources Canada, Dartmouth, Canada; 3. Department of Earth and Environmental Sciences, University of Ottawa, Ottawa, Canada, https://orcid.org/0000-0003-2364-9454 (PA); 4. Department of Earth, Ocean and Atmospheric Sciences, University of British Columbia, Vancouver, Canada; 5. Department of Earth Sciences, Simon Fraser University, Burnaby, Canada; 6. Centre de recherche GEOTOP, Département des sciences de la Terre et de l'atmosphère, Université du Québec à Montréal, Montréal, Canada, https://orcid.org/0000-0003-0967-7248 (FAD); 7. Department of Physics and Astronomy, University of Victoria, Victoria, Canada, https://orcid.org/0000-0003-2384-7370 (SED); 8. Department of Earth Sciences, University of Manitoba, Winnipeg, Canada, https://orcid.org/0000-0002-6938-6007 (AWF); 9. Department of Earth Sciences, University of Toronto, Toronto, Canada, https://orcid.org/0000-0002-1071-2314 (QL); 10. Department of Earth and Planetary Sciences, McGill University, Montréal, Canada, https://orcid.org/0000-0002-5323-8077 (YL); 11. Geological Survey of Canada, Pacific Division, Natural Resources Canada, Sidney, Canada, https://orcid.org/0000-0002-1286-5883 (AJS); 12. Department of Earth Sciences, Memorial University of Newfoundland, St. John's, Canada, https://orcid.org/0000-0002-5919-5303 (JKW)

*Corresponding author: el430484@dal.ca

Copyright © 2026. The Authors. This is an open access article distributed under the terms of the CC-BY license, which permits unrestricted use, distribution, and reproduction in any medium, provided the original work is properly cited.

Downloaded from pubs.geoscienceworld.org/ssa/srl/article-pdf/doi/10.1785/0220260156/8340850/srl-2026156.1.pdf by Dalhousie Univ Libraries Serials/Killam Library user on 23 October 2026

of measuring teleseismic earthquake phases at periods of ≤100 s for larger scale imaging were deployed for 6–7 months in the MELT experiment (Forsyth and Chave, 1994). Modern OBS, with broadband sensors (flat instrument response ~100 s to 100 Hz) capable of operating continuously for a year or more, were first developed in the late 1990s (Kanazawa *et al.*, 2001; Suetsugu and Shiobara, 2014). As major seismic zones are most often offshore, these broadband OBS have quickly become a critical data source for seismologists. Whereas modern short-period OBS (now capable of longer deployments) remain sufficient for local earthquake monitoring (Todd *et al.*, 2018; Hutchinson *et al.*, 2019) and crustal tomography (Hutchinson *et al.*, 2023), broadband OBS can additionally image larger-scale structures with both teleseismic earthquake arrivals (Hawley *et al.*, 2016; Wamba *et al.*, 2021) and ambient noise (Hable *et al.*, 2019; Harmon *et al.*, 2020). In Canada, the vast majority of earthquake hazard occurs offshore, including from the Cascadia subduction zone (Walton *et al.*, 2021) and Queen Charlotte plate boundary (Hyndman, 2015) on the Pacific Coast; the Beaufort Sea (Audet *et al.*, 2010) and Baffin Bay (Bent and Voss, 2022) seismic zones in the Arctic; and the Lower St. Lawrence (Plourde and Nedimović, 2021; Liu *et al.*, 2026), Laurentian Slope seismic zone (LSSZ), and Laurentian Fan seismic zone (LFSZ) in the Atlantic (Bent, 1995). Studies of modern seismicity in these offshore regions relying on terrestrial seismic networks are limited by large source–receiver distances and poor azimuthal coverage. International collaborations had provided some OBS coverage in the Canadian portion of Cascadia (Obana *et al.*, 2014; Toomey *et al.*, 2014), but until recently the majority of these seismic zones had never been studied with long-term broadband OBS. Therefore, Canadian seismologists identified a need for modern OBS instrumentation to monitor seismicity, as well as to image crustal and lithospheric structure in these offshore seismic zones. This led to the creation of the National Facility for Seismological Investigations (NFSI) in 2017 (Nedimović, 2019), which now operates >100 OBS across multiple deployments each year.

A drawback of OBS, from the perspective of those studying earthquakes and tectonics, is that their seismograms are typically noisy compared with those from onshore seismometers (Janiszewski *et al.*, 2022). However, this extra "noise" is useful data to a variety of physical and biological oceanographic studies. On broadband OBS, horizontal currents along the seafloor are a dominant noise source at low frequencies, and variations in the amplitude and polarization of this noise can illuminate ocean dynamic processes such as internal tides (Chang *et al.*, 2016; Ramakrushana Reddy *et al.*, 2020; Wang *et al.*, 2022) at depths where direct measurements are sparse. At higher frequencies, OBS commonly record noise from passing ships (Trabattoni *et al.*, 2023) as well as baleen whale calls (e.g., Harris *et al.*, 2013). Passive acoustic monitoring (PAM) is a primary method for monitoring endangered whale species, as it provides long-term, noninvasive observations of their distribution and behavior (Mellinger *et al.*, 2007; Van Parijs *et al.*, 2009). OBS-based whale studies regularly extend from merely detecting vocalizations to localizing and tracking individuals (Gaspà Rebull *et al.*, 2006; Dunn and Hernandez, 2009; Wilcock, 2012). OBS have lower sampling rates than typical PAM hydrophones, so they only record low-frequency calls (≲100 Hz) and are therefore only suitable for monitoring larger species, such as fin whales (*B. physalus*) and blue whales (*B. musculus*). However, OBS generally record continuously for ~12 month deployments, whereas autonomous PAM deployments commonly last from several weeks to several months, with recorders operating at high sampling rates often employing duty-cycling to extend deployment duration by conserving battery power and storage capacity (Sousa-Lima *et al.*, 2013; Stanistreet *et al.*, 2016). Therefore, OBS have tremendous potential to supplement PAM data for monitoring habitat use and ultimately support the development of conservation measures to protect baleen whales from human-caused threats (Gibb *et al.*, 2019; Davis *et al.*, 2020).

Laurentian Fan seismic zone

The southeastern margin of Canada was created by Jurassic rifting associated with the separation of Africa and North America and has since experienced thermal subsidence and extensive sedimentation (Keen and Hyndman, 1979; Pe-Piper and Piper, 2004). It has more seismicity than many comparable rifted margins (Adams and Basham, 1989), most notably producing the 1929 M_s 7.2 "Grand Banks" earthquake (Bent, 1995), which triggered a major submarine slump and turbidity current (~200 km^3; Piper *et al.*, 1988, 1999) and subsequently caused a tsunami that resulted in 28 fatalities on the Burin Peninsula of southern Newfoundland (Ruffman and Hann, 2006). The shaking from the earthquake was widely felt in eastern Canada and the northeastern United States (Lamontagne and Burke, 2018), and the slumping and turbidity current disrupted trans-Atlantic communications by severing twelve seafloor telephone cables (Doxsee, 1948).

The Grand Banks earthquake occurred at the continental margin within the Laurentian Channel, which is the most significant glacial trough in North America, extending over 1000 km landward to the St. Lawrence Estuary (Normandeau *et al.*, 2020). Modern earthquake rates in the source region of the Grand Banks event are much higher than average on the margin, and a zone of elevated earthquake rates extends seaward along-dip across the continental slope and rise, transitioning from hyperextended continental crust toward oceanic lithosphere beneath the Laurentian Fan (Fig. 1). Following the Canadian National Seismic Hazard Model (Kolaj *et al.*, 2020), we refer to the area around the Grand Banks earthquake, near the continental margin, as the LSSZ and the portion further offshore as the LFSZ (Fig. 1). The degree to which modern seismicity in the LSSZ can be considered an extended aftershock

Downloaded from pubs.geoscienceworld.org/ssa/srl/article-pdf/doi/10.1785/0220260156/8340850/srl-2026156.1.pdf by Dalhousie Univ Libraries Serials/Killam Library user on 23 October 2026

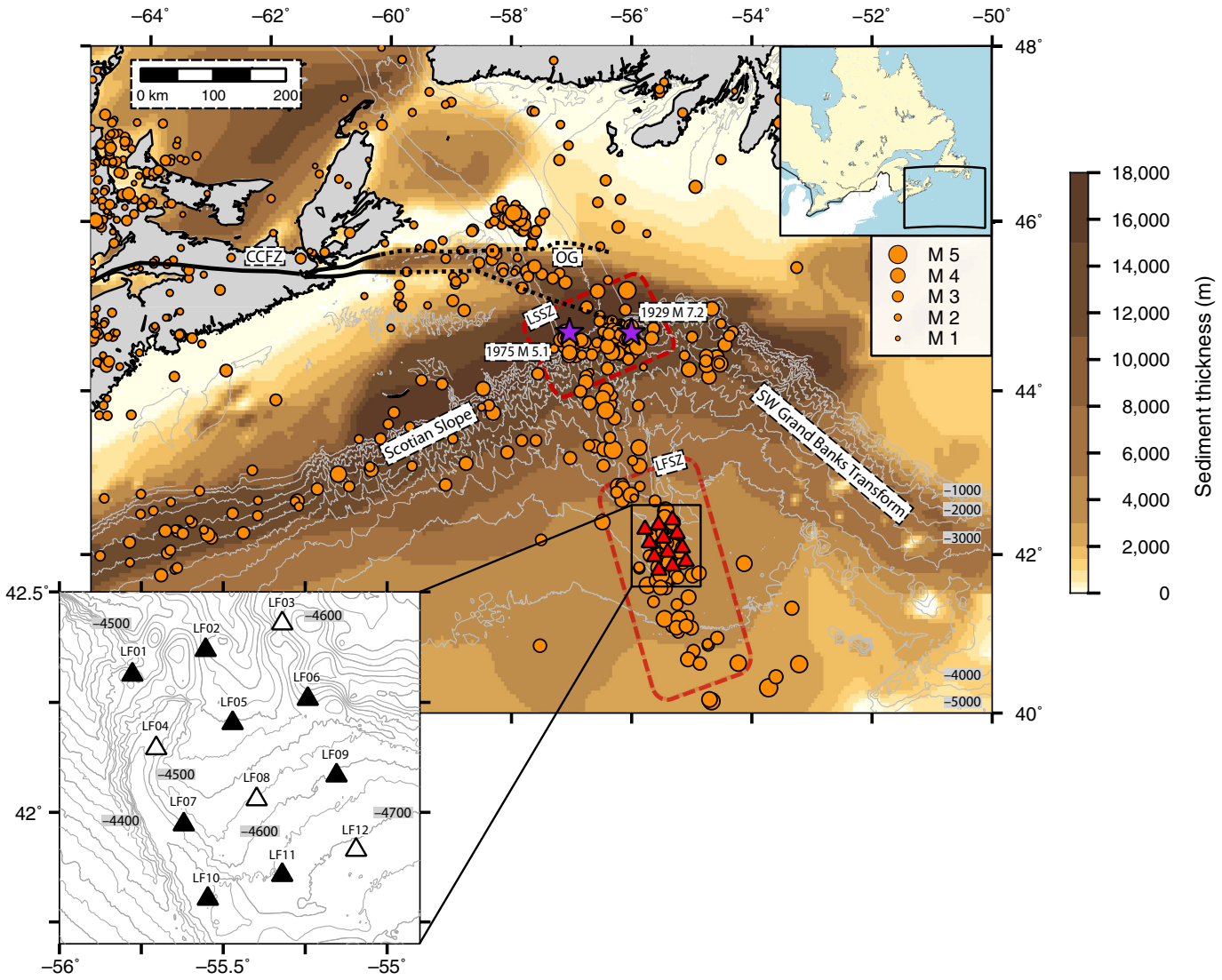


Figure 1. Sediment thickness distribution offshore southeastern Canada. Bathymetric contours are shown in gray at 500 m intervals, with finer 200 m spacing on the continental shelf; contour labels indicate depth values (m). The orange circles denote earthquakes from the National Earthquake Database of Canada (NEDB; Natural Resources Canada, 1985), recorded by land-based stations between 1985 and 2025, with symbol size proportional to magnitude ($-0.3 < M_N < 4.7$). The red triangles denote the 12 deployed ocean-bottom seismometer (OBS) stations. The Laurentian slope and Laurentian Fan seismic zones are outlined by red dashed lines and labeled as LSSZ and LFSZ, respectively. The Cobequid–Chedabucto fault zone (CCFZ) is shown as solid lines, and dashed lines indicate inferred continuations through the Orpheus Graben (OG) based on Hasegawa and Kanamori (1987). The approximate location of the southwest (SW) Grand Banks Transform is adapted from Pe-Piper and Piper (2004). The purple stars indicate the locations of the 1929 Grand Banks earthquake (Bent, 1995) and the 1975 Laurentian Channel earthquake (Hasegawa and Hermann, 1989). The Newfoundland fracture zone lies east of the study area and extends into the North Atlantic Ocean, although it is not shown. The top inset map offers a regional overview of the study area. The bottom inset map shows an enlarged view, with recovered stations in black and lost stations in white. Station names are labeled, and bathymetric contours (m) delineate the channel geometry at the deployment location. The color version of this figure is available only in the electronic edition.

sequence of the 1929 event remains ambiguous, as does whether a similar earthquake could occur elsewhere on the margin of eastern North America (Basham and Adams, 1983). Although the LFSZ forms a semicontinuous zone of seismicity with the LSSZ, the two zones do not appear to share a common major structure. Bent (1995) models the 1929 event as a primary rupture on a southeast (SE)-striking strike-slip fault, followed by two subevents on conjugate, west-southwest-striking strike-slip faults. They note that the 1929 epicenter and its principal SE-striking (122°) fault align with the Newfoundland fracture zone. Pe-Piper and Piper (2004) refer to the section of fault zone between those two structures as the southwest (SW)

Downloaded from pubs.geoscienceworld.org/ssa/srl/article-pdf/doi/10.1785/0220260156/8340850/srl-2026156.1.pdf by Dalhousie Univ Libraries Serials/Killam Library user on 23 October 2026

Grand Banks Transform (Fig. 1), noting that it appears to link to the Orpheus Graben, the continental Cobequid–Chedabucto fault system to the west, and the oceanic Newfoundland fracture zone to the east, and they suggest that these structures collectively accommodated dextral motion in the Cretaceous and Oligocene. However, the LFSZ is ~200 km south of the trend of these features and strikes south-southeast, exhibiting no clear structural relation.

The LFSZ produces more small earthquakes than the LSSZ, but it has also had a higher historical *b* value (Kolaj *et al.*, 2023). In contrast to the LSSZ's ≥ 6 earthquakes of $M > 5$ in the last century (e.g., Hasegawa and Hermann, 1989), no $M > 5$ events have been recorded in the LFSZ in the Canadian National Earthquake Database (NEDB; Halchuk *et al.*, 2015). We also note the complete absence of earthquakes in the NEDB on the SW Grand Banks Transform Margin.

The Laurentian Fan's current morphology has developed over the past 2–3 m.y. of glacial and depositional history (Stow, 1981), including the 1929 event and another 1.5 ka landslide that are among the largest Late Holocene failures globally (Normandeau *et al.*, 2019). A large positive gravity anomaly over the Laurentian Fan indicates this deposition is isostatically uncompensated (Courtney and Piper, 1992). The impact of this loading on the tectonic stress field beneath the Fan, within the oceanic lithosphere, may also contribute to the LFSZ's existence, but it is not clear whether this would be operating on the timescales of millions of years as a response to the entire depositional history of the Fan, thousands of years in response to its extensive postglacial deposits, or merely a century in response to the 1929 landslide.

This article summarizes the NFSI's first long-term OBS deployment, which took place in 2021–2022 over the LFSZ offshore Newfoundland and Nova Scotia in Atlantic Canada. It includes descriptions of the equipment used, the deployment and recovery cruises, data quality-control steps, seismic noise characteristics, and the detection and location of both earthquakes and baleen whales.

OBS Data Acquisition

Instrumentation

In January 2021, the NFSI officially reached an agreement with Güralp Systems Ltd. to acquire 120 Aquarius broadband OBS, and it has since accepted all 120 in batches between August 2021 and April 2024. The Laurentian Fan deployment represented the first long-term test of the Aquarius OBS using the initial batch of instruments. The Aquarius offers a compact, free-fall design that is fully operational at any tilt angle and is rated to a maximum water depth of 6000 m (Fig. 2a). It has the battery life and data storage capacity to record seismic data for up to 18 months before entering hibernation mode, although to date NFSI has not deployed them for longer than 14 months. The three-component seismometer has a sampling rate of 250 Hz, a 24-bit dynamic range, and a flat instrument response between 0.01 and 100 Hz, making it suitable for capturing local, regional, and teleseismic earthquakes as well as controlled sources. The internal clock is based on a voltage-controlled crystal oscillator (VCXO) and, at a stable temperature, is expected to drift less than a millisecond per day. A summary of the Aquarius OBS technical specifications is provided in Table S1, available in the supplemental material to this article.

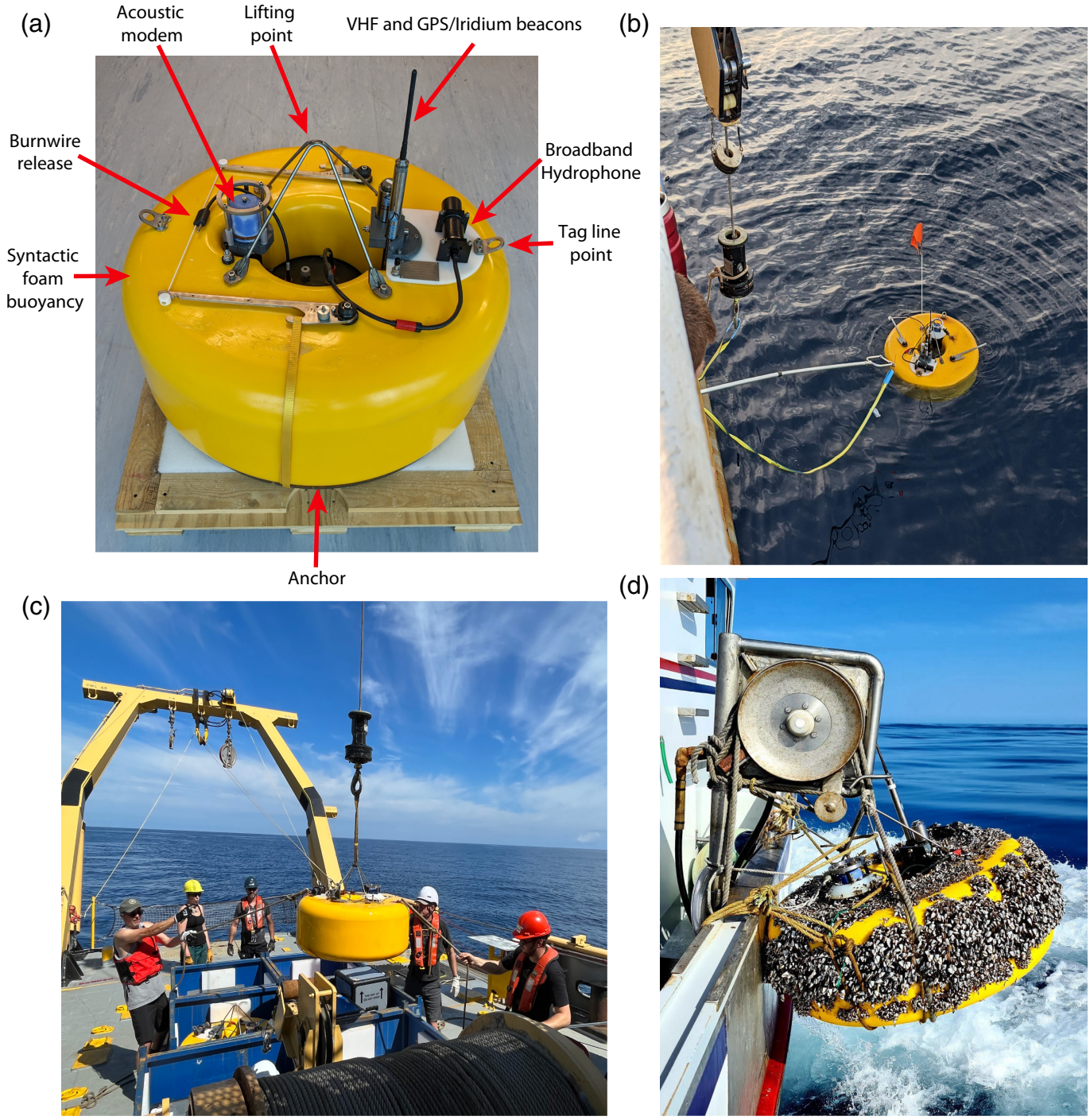
In addition to the seismometer, the Aquarius is internally equipped with a three-axis magnetometer and a microelectromechanical systems accelerometer, as well as internal and external temperature gauges (where the external gauge is in contact with the pressure case). As the instrument is not self-leveling, the internal accelerometer can be used to determine the instrument tilt after deployment and again immediately before recovery while the OBS is situated on the seafloor. Externally, it has a pressure sensor with reported accuracy of 0.25% to determine water depth and can be equipped with an additional absolute pressure gauge or hydrophone. For this study, the OBS were equipped with HighTech HTI-04-PCA ultra-low-frequency hydrophones that were set to a gain of −146 dB (50 nV/μPa), which was far too high for the oceanic setting, causing the signal to saturate rapidly and not recover, resulting in unusable data. The hydrophones have since been retrofitted to use a lower gain for subsequent deployments.

The Aquarius includes an integrated Sonardyne low-medium frequency (LMF) band acoustic modem for communication with surface vessels while at the seabed. An omnidirectional or directional dunker or ultrashort baseline (USBL) acoustic system is used to communicate with the instrument and determine its position on the seafloor. To assist in recovery of the OBS, the NFSI utilizes Xeos Apollo Mono Iridium Global Positioning System (GPS) beacons and XMB-11K very-high frequency (VHF) band radio beacons. The Apollo Mono transmits its GPS position via the Iridium satellite network; communication longevity will depend on update frequency and sea conditions, potentially tracking a drifting instrument for more than a year with daily updates.

Deployment and recovery

On 7–8 November 2021, 12 OBS were deployed on the LFSZ from the R/V Strait Explorer. The original plan was to place the instruments in a 3 × 4 grid with 40 km spacing; however, stormy weather conditions provided a very short time window during which it was safe to operate. The grid spacing was reduced to 20 km, keeping the 3 × 4 shape, reducing the array's spatial extent and the time required to deploy. The 12 OBS were deployed in under 24 hr, made possible by forgoing the OBS positioning surveys and leaving that task to the recovery cruise. Acoustic communication with the OBS was maintained for the first few hundred meters of their descent (at ~0.6 ms^{-1}) to verify that the instrument appeared to be operating normally and to reset the backup timed release to a time later than the expected recovery cruise. The 12 OBS stations,

Downloaded from pubs.geoscienceworld.org/ssa/srl/article-pdf/doi/10.1785/0220260156/8340850/srl-2026156.1.pdf by Dalhousie Univ Libraries Serials/Killam Library user on 23 October 2026



named LF01–LF12, are shown in Figure 1 and listed in Table S2.

Nineteen days after deployment, on 26 November, OBS LF08 surfaced unexpectedly; the NFSI was notified by its Apollo recovery beacon. A second OBS, LF04, surfaced three days later, and a third, LF03, surfaced on 21 December. Their GPS beacons were configured to provide only one location per day to conserve battery life, and through these daily updates, they were tracked as they slowly drifted east across the Atlantic. In May 2022, almost five months after it surfaced, LF04 was drifting near the Azores in the eastern Atlantic. The NFSI

Figure 2. (a) Güralp Aquarius OBS in the lab. The syntactic foam buoyancy with the ballast unit is 1 m in diameter and 0.46 m high, increasing to 0.72 m with the lifting frame attached. (b) Recovery of the OBS from the research vessel using a "Happy Hooker" retrieval pole to thread a lifting strap through the lifting frame before (c) hoisting the instrument onboard using the ship's crane. (d) OBS recovered near the Azores in May 2022, after drifting across the Atlantic Ocean for 5 months. The color version of this figure is available only in the electronic edition.

Downloaded from pubs.geoscienceworld.org/ssa/srl/article-pdf/doi/10.1785/0220260156/8340850/srl-2026156.1.pdf by Dalhousie Univ Libraries Serials/Killam Library user on 23 October 2026

was able to contract local fishermen to recover the instrument (Fig. 2d) and, with help from researchers at the Okeanos Institute of the Universidade dos Açores, ship it to Güralp for testing. Stations LF03 and LF08 are presumably still adrift, although the batteries in the beacons have drained below the threshold required for Iridium transmissions. Their last reported positions were near Madeira on 14 December 2022, and roughly 300 km west of Lisbon, Portugal, on 16 January 2023, respectively.

Eight of the nine remaining OBS were positioned and recovered on 29 and 30 August 2022, using the R/V Coriolis II (Fig. 2b,c). However, LF12 did not respond to acoustic communication attempts and was never recovered. Based on investigations following the recovery of LF04 and the premature surfacing of OBS from later deployments, we suspect that the OBS experienced water ingress through the connector port to the external hydrophone.

Data Quality Control

If all aspects of OBS deployment and recovery proceed smoothly, any clock drift the OBS experiences over the course of the deployment can be corrected by assuming a linear shift between GPS clock synchronizations immediately before deployment and immediately after recovery. However, in the eight OBS recovered from the Laurentian Fan, an OBS firmware issue corrupted the seismic waveforms beginning sometime on 31 January or 1 February 2022, with an approximately constant offset relative to each station's deployment time. A step increase in power consumption and internal temperature occurred at the same time (Fig. S1). Seismic data corruption was observed when searching for teleseismic earthquake signals after those dates, with signals absent or offset by seemingly unpredictable time shifts. This study, therefore, focuses on the period of slightly under three months, from 7 November 2021 to 1 February 2022. We use both teleseismic earthquakes and ambient-noise cross correlation to assess clock drift over that span. This firmware issue was corrected before later OBS deployments.

Time corrections from teleseismic *P*-wave arrivals

To assess potential clock drift, we first examine *P*-wave arrivals from teleseismic earthquakes with epicentral distances (Δ) greater than 30°. Nine events (Table S3), all with $M_w \geq 6$, were found to have sufficient signal-to-noise ratios (SNRs) on the vertical component to manually pick a *P*-wave arrival, though the horizontal components were often noisier. Using these picks, we computed station–pair travel-time double differences (Zhang *et al.*, 2010), defined as the difference between observed and theoretical differential arrival times between pairs of stations for the same event (Fig. 3a). Double-difference times up to ±5 s were considered normal due to velocity heterogeneities and picking errors, and values for most stations lie within this threshold. However, LF09 exhibited a time offset of ∼1050 s, which was corrected before moving to the next steps. This is the only instance thus far that NFSI has observed a static clock offset for an Aquarius deployment; discussion with the manufacturer has not revealed a potential cause yet. As a further check, we computed cross-correlation-based double-difference times (Poupinet *et al.*, 1984; Waldhauser and Schaff, 2007), which reduced scatter to within ±2 s (Fig. 3b).

Time corrections from ambient noise cross-correlation

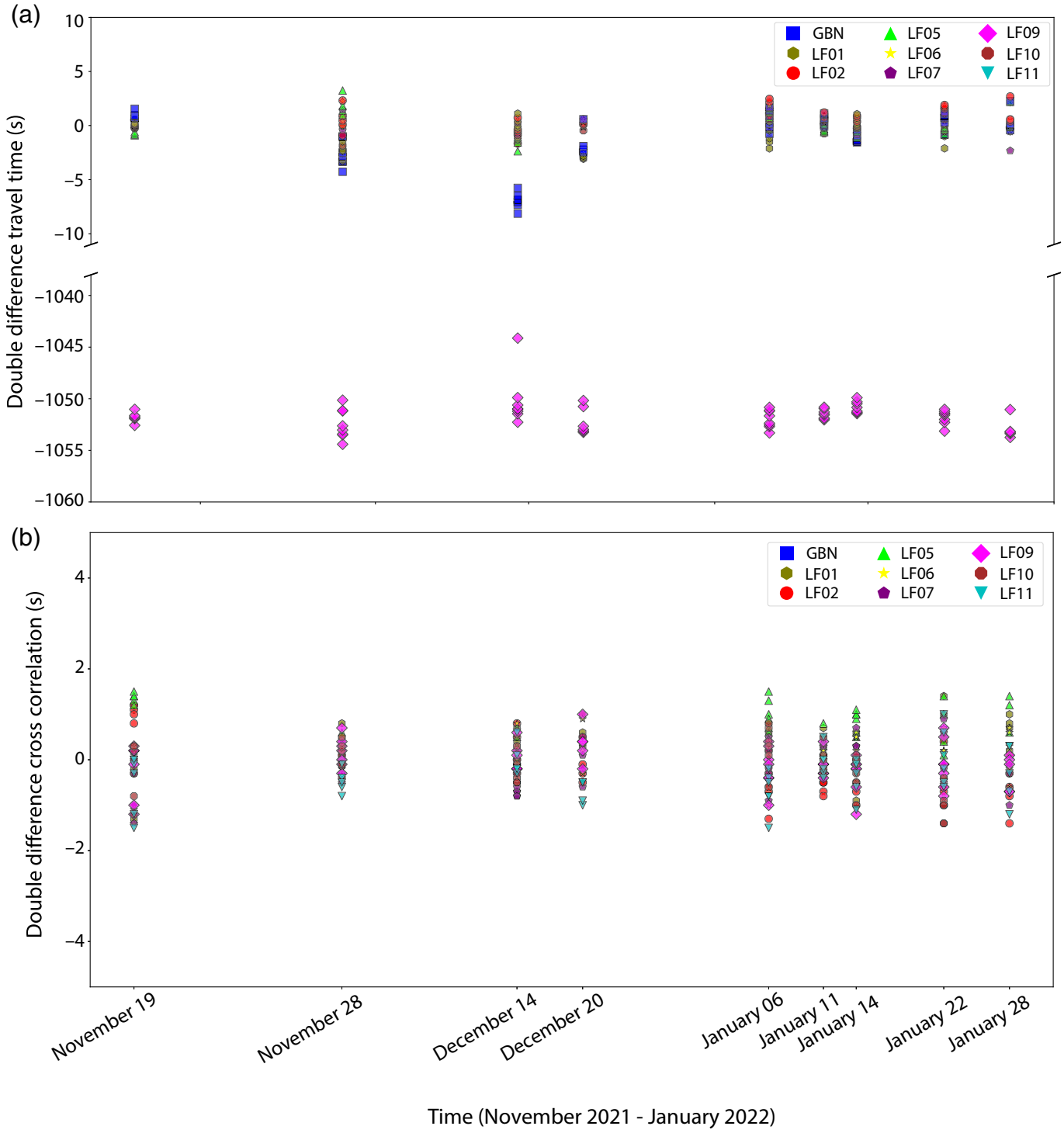
To detect potential continuous clock drift, we performed a time-symmetry analysis of ambient-noise cross-correlation functions (NCCFs). Relative clock drift can be inferred from asymmetry in the NCCF, which results in a shorter travel time at the negative-lag peak and a longer travel time at the positive-lag peak, or vice versa (Stehly *et al.*, 2007). Ideally, NCCFs are computed for all nine component pairs for each station pair; however, for simplicity and because the horizontal components exhibit higher levels of ocean noise, only the vertical components were used.

We first implemented the data preprocessing scheme presented by Bensen *et al.* (2007): (1) the data were band-pass filtered between 2 and 5 s, (2) time-domain normalization was applied to reduce the impact of earthquakes, instrumental irregularities, and nonstationary noise sources near the stations on the NCCF, and (3) spectral normalization was applied to combat NCCF degradation caused by persistent monochromatic sources. Following Abbas *et al.* (2023), we computed NCCFs from preprocessed 6 hr long traces with a 3 hr (50%) overlap between windows. The resulting NCCFs were first stacked within each day to obtain daily functions and subsequently stacked over time to highlight trends over the deployment period (Figs. S4 and S5). Figure 4 compares different station pairs and shows that seven stations do not exhibit significant clock drift, whereas LF02 displays a distinct drift relative to the others. We applied the multichannel cross-correlation technique (VanDecar and Crosson, 1990), using station–pair total relative clock drifts as input, to estimate an optimal and self-consistent set of clock drift rates for each station. Because LF02 was identified as anomalous, it was excluded from the zero-sum constraint; that is, the sum of drifts for the remaining seven stations was constrained to equal zero. This resulted in a total clock drift of 1.14 s for LF02, whereas the other stations exhibited drifts of less than ±0.1 s. The clock drift on LF02 was corrected by incrementally adjusting the start time of each daily seismogram (13 ms per day), whereas the smaller drifts on the other stations were negligible relative to the uncertainty in NCCF-derived travel times and observed residual scatter.

Instrument orientation and tilt estimation

OBS deployed via free fall have (nominally) horizontal components with unknown azimuths due to the lack of controlled

Downloaded from pubs.geoscienceworld.org/ssa/srl/article-pdf/doi/10.1785/0220260156/8340850/srl-2026156.1.pdf by Dalhousie Univ Libraries Serials/Killam Library user on 23 October 2026



orientation during descent; resolving their orientations is important for various further applications. Although a variety of methods exist to estimate orientation, using the polarization of teleseismic earthquake *P*-wave arrivals (Niu and Li, 2011; Braunmiller *et al.*, 2020) is perhaps the most straightforward. This process assumes a simplified, laterally homogeneous and isotropic Earth such that energy from the direct *P*-wave arrival is constrained to the vertical and radial (*P* and *SV*) components, with negligible energy in the transverse (*SH*) component. We found that only four events ($M_w \geq 6.8$, $\Delta > 30°$)

Figure 3. Station–pair double-difference analysis results for OBS stations. (a) Travel-time double-difference residuals for nine teleseismic events recorded from November 2021 to February 2022 across eight stations. (b) Cross-correlation-based double-difference residuals for the same period and station pairs. Residuals are computed between pairs of stations for each event. Each station is represented by a unique marker, with pairwise combinations yielding seven observations per station. Results are plotted over time, highlighting variations and trends in both travel-time and cross-correlation residuals. The color version of this figure is available only in the electronic edition.

Downloaded from pubs.geoscienceworld.org/ssa/srl/article-pdf/doi/10.1785/0220260156/8340850/srl-2026156.1.pdf by Dalhousie Univ Libraries Serials/Killam Library user on 23 October 2026

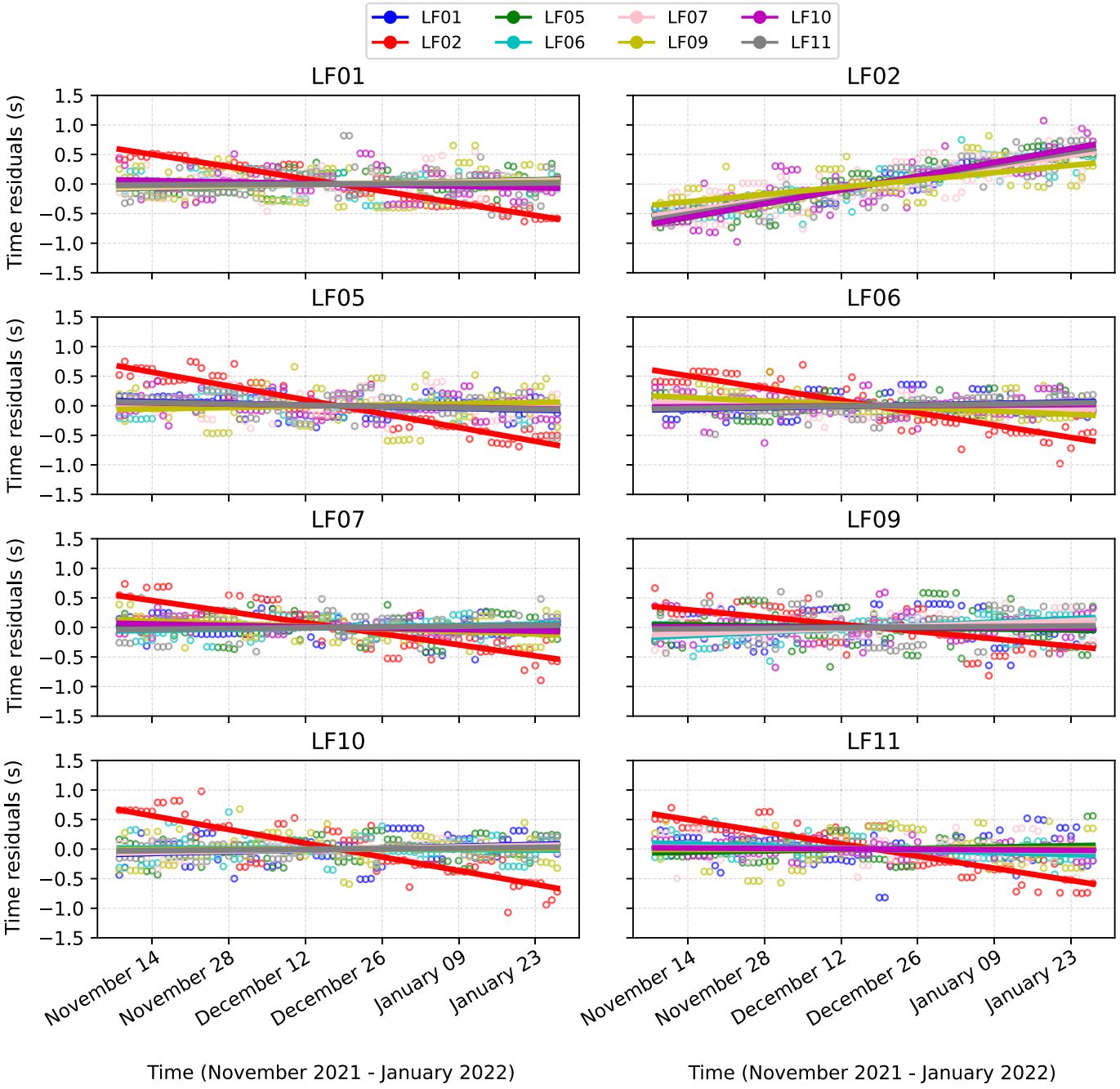


Figure 4. Ambient-noise cross-correlation function (NCCF) results and inferred clock drift for OBS stations from November 2021 to February 2022. Each subplot shows time shifts derived from NCCFs between one reference station and all other stations. Scatter points represent daily measurements, and solid lines indicate linear fits used to estimate clock drift rates. The trends highlight relative timing variations between stations over the deployment period. The color version of this figure is available only in the electronic edition.

had sufficient SNR on the horizontal components to be included in this analysis. We performed a line search over potential orientations from 0° to 360°, maximizing energy on the radial component while ensuring a positive cross-correlation between the radial and vertical components. An example of the rotation from the original horizontal components to radial and transverse components for a teleseismic event is provided in Figure S6. We used a 45 s window beginning at a manual *P* arrival pick and varied the band pass slightly between arrivals, from 0.02–0.06 Hz to 0.04–0.08 Hz, depending on the event magnitude and observed SNR. The SNR for each station was calculated from the horizontal components using 120 s of prearrival noise and 45 s of postarrival signal windows. Results of the line search are shown in Figure 5 and summarized in Table 1 with median SNR reported in decibels. With only four events, it is challenging to establish a

Downloaded from pubs.geoscienceworld.org/ssa/srl/article-pdf/doi/10.1785/0220260156/8340850/srl-2026156.1.pdf by Dalhousie Univ Libraries Serials/Killam Library user on 23 October 2026

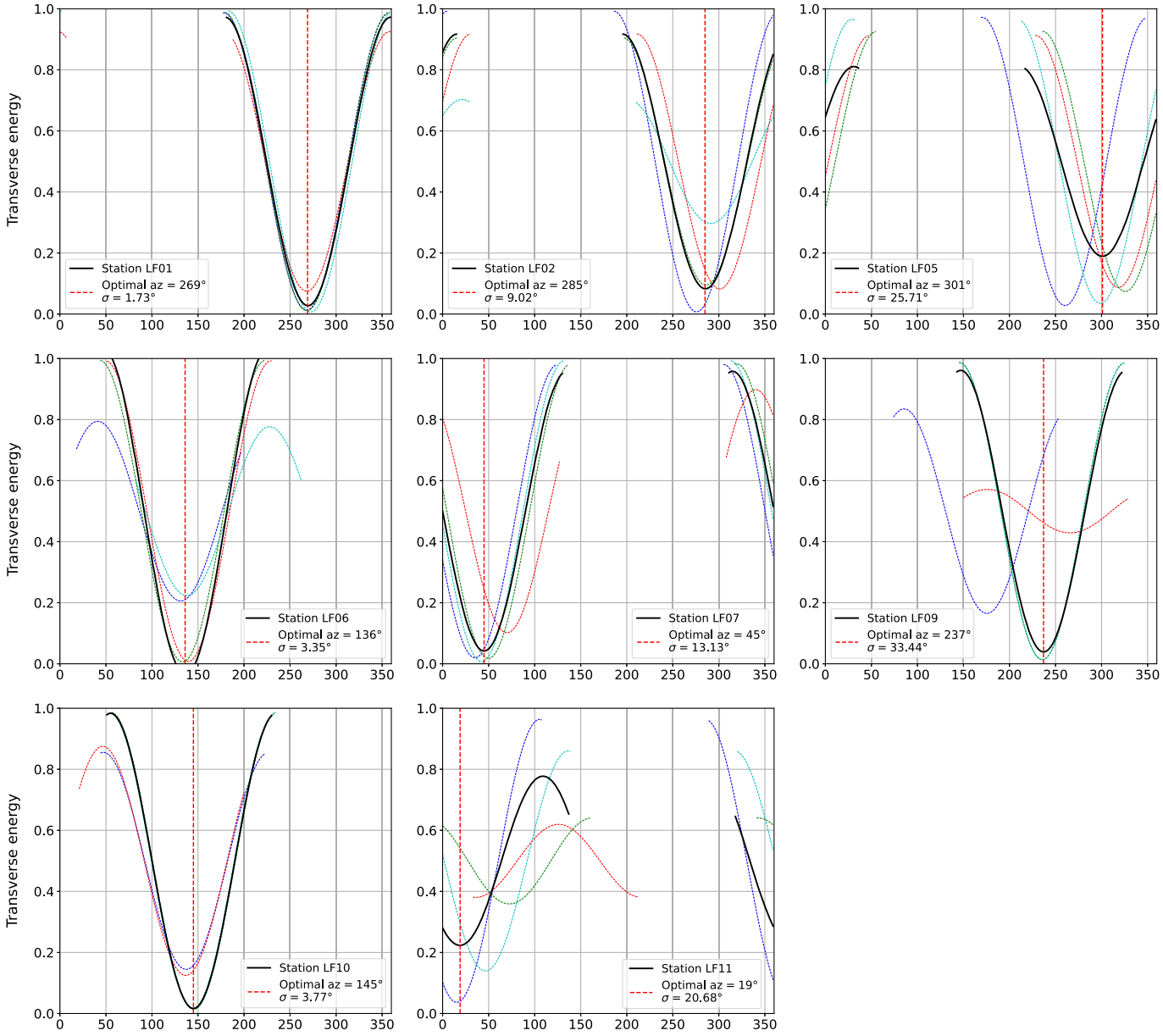


Figure 5. Optimal orientation results for eight OBS stations using four teleseismic events. Each subplot shows transverse energy as a function of the assumed azimuth of the H2 horizontal component. The colored curves correspond to individual events, and the black curve represents the stacked transverse energy, with solutions restricted to positive radial–vertical cross-correlation. The red vertical line indicates the azimuth that minimized transverse energy, interpreted as the optimal orientation of the H2 component. The color version of this figure is available only in the electronic edition.

meaningful uncertainty measure, but the visual spread of minima positions for each OBS suggests uncertainties ranging from a few degrees for the highest-SNR stations to ~20° for the lowest-SNR stations.

Because of the free-fall deployment method, OBS may land on a rough or sloping seafloor or sink unevenly into soft seafloor sediments, resulting in the seismometer components being tilted from their nominal horizontal and vertical directions. The effect of this tilt can be corrected in the seismic data to reduce low-frequency tilt noise on the vertical component. Note that the term "tilt noise" has a double meaning: (1) it describes the noise on the seismometer produced as bottom currents flow past the OBS and induce Kármán vortex shedding that deforms the underlying sediments and (dynamically) tilts the instrument frame (Duennebier and Sutton, 1995; Webb, 1998; Stähler *et al.*, 2018), and (2) because this effect is negligible on a truly vertical component, noise data can be analyzed to determine an overall (static) instrument tilt and remove tilt noise from the nominally vertical component (Crawford and Webb, 2000).

We estimated the tilt angle and direction of each OBS using the ATaCR module of the OBStools package (Audet and Janiszewski, 2020), which applies the transfer function approach

Downloaded from pubs.geoscienceworld.org/ssa/srl/article-pdf/doi/10.1785/0220260156/8340850/srl-2026156.1.pdf by Dalhousie Univ Libraries Serials/Killam Library user on 23 October 2026

TABLE 1
Orientation and Tilt Estimates for Eight OBS Stations

Station	H1 Azimuth	H2 Azimuth	Std	Med. SNR	Tilt	Tilt Dir.
LF01	179	269	1.7	21.4	0.9	337
LF02	195	285	9.0	19.6	1.1	126
LF05	211	301	25.7	13.4	19.1	344
LF06	46	136	3.4	8.1	3.0	305
LF07	315	45	13.1	12.1	4.8	342
LF09	147	237	33.4	14.1	0.7	96
LF10	55	145	3.8	10.3	3.4	119
LF11	289	19	20.7	2.3	1.9	300

Listed are the azimuths of the horizontal components (H1 and H2), the circular standard deviation (Std) reflecting orientation variability, and the median (Med.) signal-to-noise ratio (SNR) for each station. The rotation required to align the recorded components with geographic north and east is given by the negative of the H1 azimuth. Also shown are the estimated tilt angles and corresponding tilt directions (Dir.), which describe the magnitude and orientation of instrument inclination, measured clockwise from the H1 component. All angular measurements are in degrees. OBS, ocean-bottom seismometer.

described by Bell *et al.* (2015). Circular statistics were applied to determine the mean tilts and tilt directions from daily estimates obtained using ATaCR (Table 1). Seven OBS exhibit a tilt angle of <5°, whereas station LF05 displays a substantially larger tilt angle of 19.1°. To validate the tilt angle estimated for station LF05, we compared the SNR of the vertical and horizontal components for teleseismic *P*-wave arrivals at frequencies below 0.1 Hz (Fig. S7). As expected, vertical components always exhibit higher SNR than horizontal components on each OBS. However, LF05 has the lowest vertical SNR and a reduced difference between vertical and horizontal SNR, supporting the notion that LF05 had an anomalously high tilt angle.

Noise characteristics

OBS are subject to a diverse set of noise sources arising from oceanic interactions, seafloor coupling conditions, and anthropogenic and natural sources (e.g., marine mammals). To quantitatively characterize the ambient noise characteristics, we calculated the probabilistic power spectral density (PPSD) following McNamara and Buland (2004). The data were segmented into 1-hr windows with 50% overlap, within the frequency band recorded by our instruments, for the three months of quality data. PPSD results for all stations are in Figures S8–S15. For reference, the figures include the new high-noise model (NHNM) and new low-noise model (NLNM) introduced by Peterson (1993), using land-based stations.

Our findings are broadly consistent with trends observed by Janiszewski *et al.* (2022), who analyzed noise characteristics from 551 OBS deployments. These findings include ambient noise that slightly exceeds the NHNM in the 0.2–1 Hz (secondary microseism) frequency band. At lower frequencies (0.01–0.1 Hz), all components exhibit high variability in noise level, but the horizontal components are much noisier than the vertical; vertical noise levels cluster near the NHNM, whereas the horizontals greatly exceed the NHNM by up to ∼40 dB. From 3 to 10 Hz, the band of interest for observing local seismicity, ambient noise falls below the NHNM but again exhibits high temporal variability (especially on stations LF09 and LF11) and remains ∼10 dB higher on the horizontals than on the vertical component.

We examined noise spectrograms created from 5 min windows with 50% overlap. Figure 6 illustrates four examples from stations LF01, LF02, LF06, and LF09. The results show a consistently elevated noise floor below 3 Hz, resulting from the presence of microseisms, infragravity waves, and bottom-current noise (Janiszewski *et al.*, 2022). Blue whale calls are observed at a frequency of approximately 16.5 Hz, whereas fin whale calls predominantly appear at 18–22.5 Hz (seen most clearly in Fig. 6c). Numerous vertical line features spanning the full range of frequencies are discernible, some of which correspond to abrupt data spikes and may be artifacts.

At some stations, an arc-like pattern appears in the spectrogram immediately after deployment, characterized by a step-like increase in noise levels above a given frequency threshold. This threshold changes rapidly over the first few days before gradually stabilizing, as seen in Figure 6a at 40 to 70 Hz. This behavior may be related to thermal adjustments within the OBS, consistent with similar trends observed in internal humidity and pressure records (Figs. S2 and S3).

Below 0.1 Hz, tilt noise dominates, and the horizontal components exhibit significantly higher noise levels than the vertical on most OBS (>25 dB difference), although the highly tilted LF05 has more vertical noise, and the horizontal noise amplitudes are more comparable (Figs. S16–S23). Seafloor compliance noise is expected to be present on the vertical component, but at frequencies below 0.02 Hz for this water depth (Crawford and Webb, 2000), which is too low to be observed in PPSD in Figures S8–S15. Because frequencies below 0.1 Hz are

Downloaded from pubs.geoscienceworld.org/ssa/srl/article-pdf/doi/10.1785/0220260156/8340850/srl-2026156.1.pdf by Dalhousie Univ Libraries Serials/Killam Library user on 23 October 2026

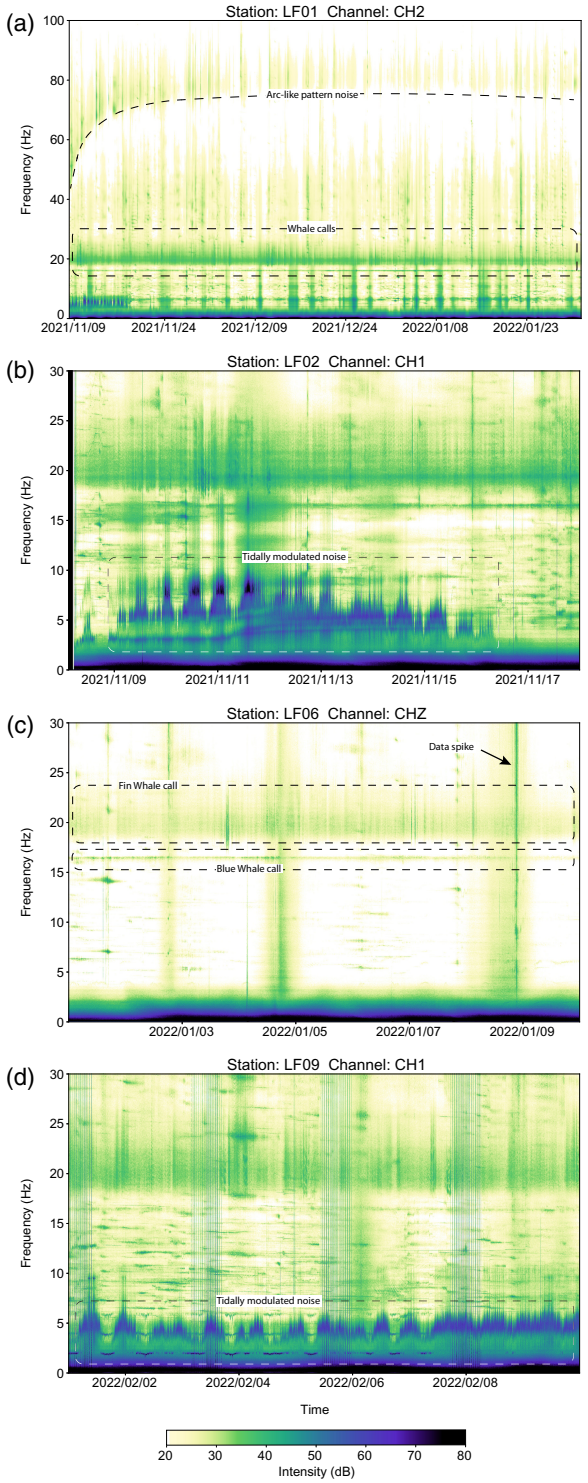


Figure 6. Spectrograms from stations LF01, LF02, LF06, and LF09 during selected time periods. (a) Station LF01, horizontal component, 0–100 Hz for 87 days of uncorrupted data. (b) Station LF02, horizontal component, 0–30 Hz for 10 days. (c) Station LF06, vertical component, 0–30 Hz for 10 days. (d) Station LF09, horizontal component, 0–30 Hz for 10 days. Note that the higher and lower limits of the colorbar were set to 20–80 dB to help visually highlight and contrast interesting features. The color version of this figure is available only in the electronic edition.

not relevant to our subsequent analyses, we opt not to correct for tilt or compliance noise; we also lack the hydrophone data required to perform compliance correction.

Between approximately 4 and 10 Hz, periods of elevated noise persisting over several days are observed at most stations (Fig. 6b,d) and are likely related to strong, transient seafloor currents. These signals appear to be modulated at a semidiurnal period, suggesting an influence from internal tides, as previously observed on continental slopes (Ramakrushana Reddy *et al.*, 2020), including the North American Atlantic margin (McGregor, 1979). Noise in this band includes broadband signals as well as signals with a strong characteristic frequency (~2 Hz in Fig. 6d) and its harmonics. These signals may be related to resonance of the OBS–sediment coupling (Sutton *et al.*, 1981; Trehu, 1985), shear-wave resonance within the sedimentary sequence (Godin and Chapman, 1999), and/or vortex shedding off the OBS or one of its external components (Essing *et al.*, 2021; Corela *et al.*, 2023). The OBS were deployed on several kilometers of sediment, which may enhance seafloor resonance. Based on the wide-angle seismic velocity model of Lau *et al.* (2018), the sedimentary section in this region is approximately 4 to 5 km thick, including an upper ~3 km with $V_P < 3$ km s^{-1}, consistent with Quaternary unconsolidated sediments (Piper *et al.*, 1983; Fig. 1).

Earthquake Detection and Location

To begin building an earthquake catalog, we first applied OBSTransformer (Niksejel and Zhang, 2024), a generalized transfer-learned *P*- and *S*-phase picker designed specifically for OBS data. We selected *P*- and *S*-picking probability thresholds of 0.1 and obtained 31,863 *P* picks and 87,312 *S* picks from the three months of seismic data. These picks were then input into the Rapid Earthquake Association and Location code (REAL, Zhang *et al.*, 2019), assigning a minimum of three *P*, one *S*, and five total picks per event. The grid search for potential hypocenters spanned 6° in both horizontal directions and 40 km in depth, with grid intervals of 0.1° horizontally and 2 km vertically. We derived a 1D velocity model (Table S4) from the 2D *P*-wave velocity model of Lau *et al.* (2018), computed from a dense wide-angle seismic survey across the northeastern Nova Scotia margin, approximately 50 km west of our OBS array at its closest point. The model includes 4.8 km of sediments overlying a 5.6-km-thick igneous crust, for a Moho depth of 10.4 km relative to the seafloor. We applied the Wadati and Oki (1933) method to estimate an average V_P/V_S for the study area, resulting in an optimal V_P/V_S near 1.7 but with very high uncertainties (95% confidence interval: 1.57–2.07; Fig. S24). We expected a higher V_P/V_S because the OBS sit on several kilometers of un- to poorly consolidated sediments, although it may be that the Wadati analysis is insensitive to the sediments if all arrivals traverse them with similar near-vertical ray-paths. Given these uncertainties, we opted to apply a constant standard V_P/V_S of 1.75.

Downloaded from pubs.geoscienceworld.org/ssa/srl/article-pdf/doi/10.1785/0220260156/8340850/srl-2026156.1.pdf by Dalhousie Univ Libraries Serials/Killam Library user on 23 October 2026

REAL output more than 100 events; however, after manual inspection and relocation using a likelihood-based hypocenter inversion code in Python, similar to NonLinLoc (Lomax *et al.*, 2000) and that of Plourde and Nedimović (2021), only 17 were confirmed to be robust detections (Fig. 7, Table S5). The NEDB catalog lists only two earthquakes near the Laurentian Fan during the time span of the OBS deployment, both of which are included among our detected events.

Estimated hypocentral depths range from near the surface to ~39 km. Only 3 of the 17 epicenters lie within the OBS array (although another 7 are within 20 km), resulting in poor azimuthal coverage for most events. The reported uncertainties rely on arbitrarily applied Gaussian uncertainties for arrival times, with higher uncertainties assigned to later arrivals, and uncertainties in the velocity structure are not accounted for. As a result, these estimates likely underestimate the true uncertainties in some cases, particularly for the most distant events and for those in which the inversion favors very shallow depths (<1 km). Such shallow earthquakes are especially unlikely in this region, where several kilometers of unconsolidated to poorly consolidated sediments are expected at the surface. The largest cluster of depths, at ~30 km, is 20 km beneath the Moho and includes 8 of the 10 events located within 20 km of the OBS. Given the computed and inferred uncertainties on shallower events, no hypocenters can be confidently interpreted as occurring within the oceanic crust.

Figure 8 shows vertical-component waveforms from the 15 December 2021 event, also recorded in the NEDB catalog, arranged by increasing station distance. This earthquake occurred more than 100 km south of the OBS array, and the body waves appear to be followed by a *T* phase, characterized by prolonged high-frequency energy trailing the surface waves observed across all stations, with an apparent moveout velocity of ~1.5 km s^{-1}. *T* waves are seismoacoustic waves generated by earthquakes that propagate efficiently within the ocean's sound fixing and ranging channel, where sound speed reaches a minimum (Linehan, 1940; Tolstoy and Ewing, 1950), and can travel long distances with minimal attenuation (Okal, 2008).

We determine local magnitudes for the 17 events in our catalog using the amplitude–magnitude relationship established by Bakun and Joyner (1984). To achieve this, the maximum amplitudes of the horizontal components are measured after removing the instrument response and convolving the resulting signals with the Wood–Anderson response. The waveform window selected for this measurement spans 10 s around the *S* wave. The detected events exhibit local magnitudes between −0.1 and 2.2, with the majority below 1.5 and only two exceeding magnitude 2.0.

Whale Detection and Location

We catalog specific types of low-frequency fin whale (*B. physalus*) and blue whale (*B. musculus*) calls that are regularly observed on OBS in the western North Atlantic. The fin whale calls are generally an ~1 s downsweep focused at ~20 Hz and repeated with an internote interval (INI) of approximately 10 to 15 s (Morano *et al.*, 2012; Roy *et al.*, 2018); whereas blue whale calls tend to consist of a constant frequency "A" phase lasting ~8 s, a downsweep "B" phase lasting ~10 s, or (most commonly) these two in succession with a ~5 s gap as an A–B sequence, generally repeating with a 68 to 78 s INI (Mellinger and Clark, 2003; Wingfield *et al.*, 2022). Although we focus on these two most abundant call types in this study, we note that a number of other calls, including some from sei and humpback whales, are potentially observable in the OBS frequency range (<125 Hz).

We applied the double-spectrogram method of Plourde and Nedimović (2022) to detect fin and blue whale calls on the Laurentian Fan OBS. This template-free approach relies on the characteristic recurrence intervals of vocalizations from each species. The workflow involves band-pass filtering the seismic data, computing a short-window spectrogram (1–2 s) to resolve individual calls, and calculating a ratio (R) of energy concentration within the target frequency band relative to adjacent control bands. A second, longer-window spectrogram is then generated from the $R(t)$ time series to assess periodic modulation of energy, and a detection is triggered when the resulting power ratio (W) exceeds an empirically defined threshold. Figure 9 displays four representative examples of detected whale calls. Analysis of the fin whale calls reveals that the INI range is between 10 and 21 s, extending beyond the 10–15 s range commonly reported for the Northwest Atlantic in previous studies (Fig. 9c).

Both blue and fin whale calls were present on most days of the deployment. Over the ~92-day dataset, blue whale calls were detected on ~86 days (averaged across the eight OBS), and fin whale calls were detected on ~63 days (Fig. S25). In total, across the eight OBS, we detected 211,568 blue whale calls and 132,768 fin whale calls, although these numbers include duplicate detections of the same call across multiple stations. As we have not associated all calls across OBS, we do not have precise numbers of unique calls. On average, each station recorded approximately 26,000 blue whale calls and 17,000 fin whale calls over the study period. Considering their average INI, these values equate to blue whale A–B songs being present in over 20% of the OBS recordings and fin whale songs being present in ~3% to 4%.

We applied a workflow similar to the earthquake catalog-building process to localize blue whale calls for one day of data (14 January 2022). Rather than manually picking each call, we relied on automatic detections from the double-spectrogram method, which tends to be at the center of a call (at the highest amplitudes). However, for blue whale A–B calls, the pick position within the call can vary by several seconds, in part because seafloor multiples are expected to overlap with the direct arrival and, for a given source–receiver distance, these multiples can have larger amplitudes than the direct

Downloaded from pubs.geoscienceworld.org/ssa/srl/article-pdf/doi/10.1785/0220260156/8340850/srl-2026156.1.pdf by Dalhousie Univ Libraries Serials/Killam Library user on 23 October 2026

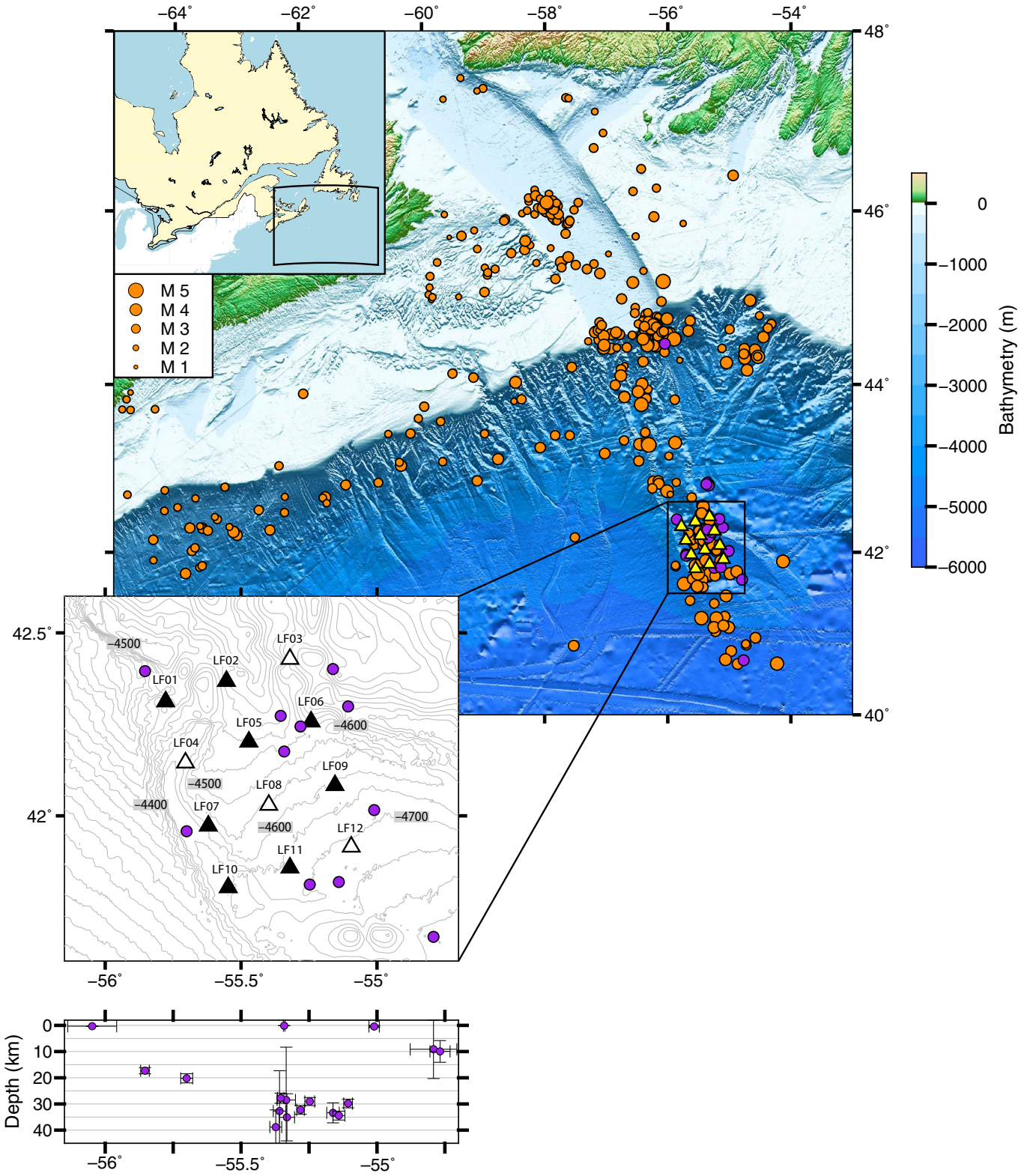


Figure 7. Seismicity map of the lower LFSZ. The orange circles denote earthquakes from the NEDB (Natural Resources Canada, 1985) recorded by land-based stations, from 1985 to 2025; purple circles represent the 17 detected events using the eight OBS stations. The triangles indicate the locations of the OBS stations. The top inset map offers a regional overview of the study area. The bottom inset map provides an enlarged view of the study area, displaying ocean depth contours (4400–4700 m). The black triangles denote the eight recovered stations, and the white triangles denote the four lost stations. The horizontal cross section at the bottom shows the depth distribution of locally detected events, with error bars representing 95% confidence intervals. The color version of this figure is available only in the electronic edition.

Downloaded from pubs.geoscienceworld.org/ssa/srl/article-pdf/doi/10.1785/0220260156/8340850/srl-2026156.1.pdf by Dalhousie Univ Libraries Serials/Killam Library user on 23 October 2026

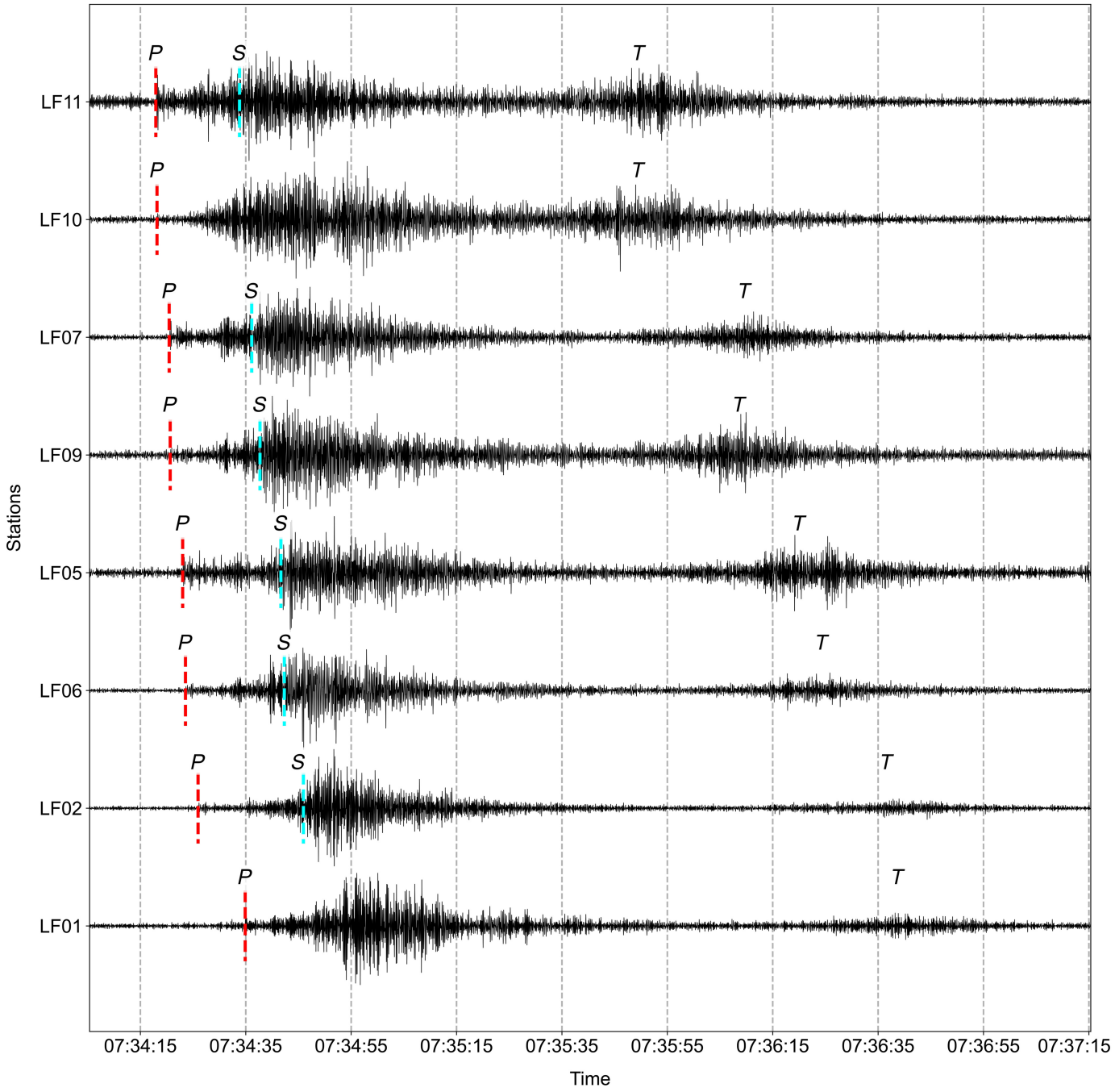


Figure 8. Example vertical-component waveforms from a detected regional earthquake, ordered by station distance to highlight the moveout pattern. This event occurred on 15 December 2021 at 07:33:59, with an estimated magnitude of 2.2 and depth of ~10 km. The red and cyan dashed lines indicate the picked arrival times of the *P* and *S* waves, respectively. The prolonged high-frequency energy observed in the trailing portion of the waveforms is interpreted as the *T* phase. The color version of this figure is available only in the electronic edition.

wave. This issue is less pronounced for the ~1 s long fin whale calls, but phase association is more complex in this case, where multiples appear as distinct phases that are often more prominent than the direct wave (and can be useful in ranging the calls, e.g., Zhu and Wen, 2024) and travel-time differentials often exceed the INI. To estimate the true onset of each whale call, we implemented a custom envelope-based picking algorithm. For each detection, the three-component waveform was combined into a smoothed signal envelope, and the onset was defined as the first sustained increase in envelope amplitude above an adaptive threshold determined from robust estimates of the background noise level and the peak signal amplitude.

The refined picks were then associated across stations with a simple sequencing approach, relying on the consistent INI and manually correcting cases where a call was not picked at a given station. To localize the recorded whale calls, we again

Downloaded from pubs.geoscienceworld.org/ssa/srl/article-pdf/doi/10.1785/0220260156/8340850/srl-2026156.1.pdf by Dalhousie Univ Libraries Serials/Killam Library user on 23 October 2026

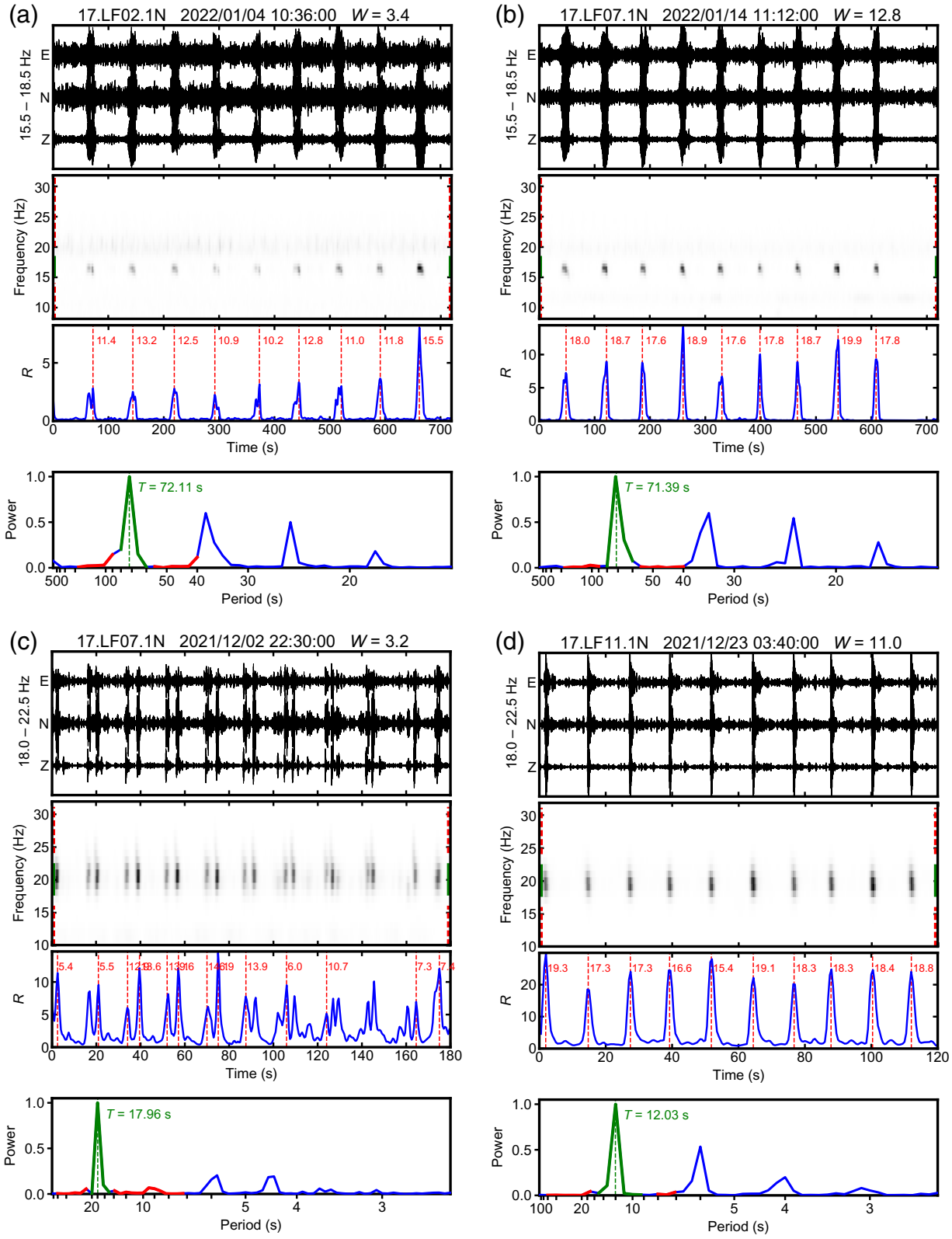


Figure 9. Example detections of (a,b) blue whales and (c,d) fin whales from stations LF02, LF07, and LF11. The top row shows the three-component seismograms, band-pass filtered to the target frequency band for each species. The second row presents the corresponding spectrograms of the same waveform segments, with a solid green line highlighting the target band and red dashed lines highlighting the adjacent bands used in the denominator of $R(t)$. In the third row, $R(t)$ is computed from the spectrograms, with detected calls labeled by red lines and annotated with their signal-to-noise ratio (SNR) in dB. The bottom row shows the periodogram of $R(t)$, with periods used in the numerator of $W(t)$ highlighted in green and those in the denominator in red. The color version of this figure is available only in the electronic edition.

Downloaded from pubs.geoscienceworld.org/ssa/srl/article-pdf/doi/10.1785/0220260156/8340850/srl-2026156.1.pdf by Dalhousie Univ Libraries Serials/Killam Library user on 23 October 2026

used a likelihood-based recursive grid-search routine, similar to NonLinLoc (Lomax *et al.*, 2000), implemented in Python. In this case, we constrained the whale source depth to be 20 m below the sea surface. We also added azimuthal constraints, derived from the first principal-component (polarization) axes of the calls, using the results of the Instrument orientation and tilt estimation section to correct for instrument orientation. The call backazimuths were only constrained to a 180° ambiguity, as polarization axes are expected to be near-horizontal in most cases (Wilcock, 2012). Standard uncertainties on pick arrival times and azimuths were assigned to 0.5 s and 10°, respectively. This workflow resulted in 501 initial event locations, shown with uncertainty ellipses in Figure S26.

To refine these absolute locations, we implemented a double-pair double-difference (DPDD) approach (Guo and Zhang, 2017). Similar to the double-difference approach (Waldhauser and Ellsworth, 2000), this method can improve relative locations by effectively cancelling errors associated with an imperfect velocity model. In our case, the main advantage of this approach is the ability to incorporate cross-correlation delay times, which we calculated using the whale call index (Širović *et al.*, 2015; Pilkington *et al.*, 2018). We constructed this index by integrating spectrogram power over a target frequency band (15.5–18.5 Hz), summed across components. Both event–pair and station–pair cross-correlation constraints are considered, and a correlation coefficient (CC) threshold of 0.8 is applied in subsequent analyses (Fig. S27). Event pairs greatly outnumber station pairs owing to the larger number of events (8 stations versus 501 events); however, their CC distributions are similar, with median values of 0.68 and 0.67, respectively.

The inversion incorporates particle-motion azimuth constraints together with time-difference constraints derived from both travel-time picks and cross-correlation measurements. As recommended by Guo and Zhang (2017), we apply station pair double-difference (SPDD) and DPDD constraints simultaneously, with both pick-based and cross-correlation-based constraints for each. DPDD constraints were formed using both cross-event and cross-station correlations. After applying a CC threshold of 0.8 and double-difference criteria, 7,621 station–pair and 10,729 event–pair cross-correlation constraints were retained for the hybrid relocation. To construct event pairs for the inversion, we employed a temporal nearest-neighbor approach to identify pairs likely to exhibit high coherence. The resulting sparse system of equations was solved using damped least squares, with adaptive weighting based on pick uncertainties, cross-correlation coefficients, and a robust Tukey biweight function to suppress outliers. The inversion weighting structure began with the highest weights on azimuthal, SPDD, and pick-based constraints and gradually shifted weight to the cross-correlation and DPDD constraints.

Figure 10 illustrates the relocation results, depicting the movement of a blue whale for one day on 14 January 2022,

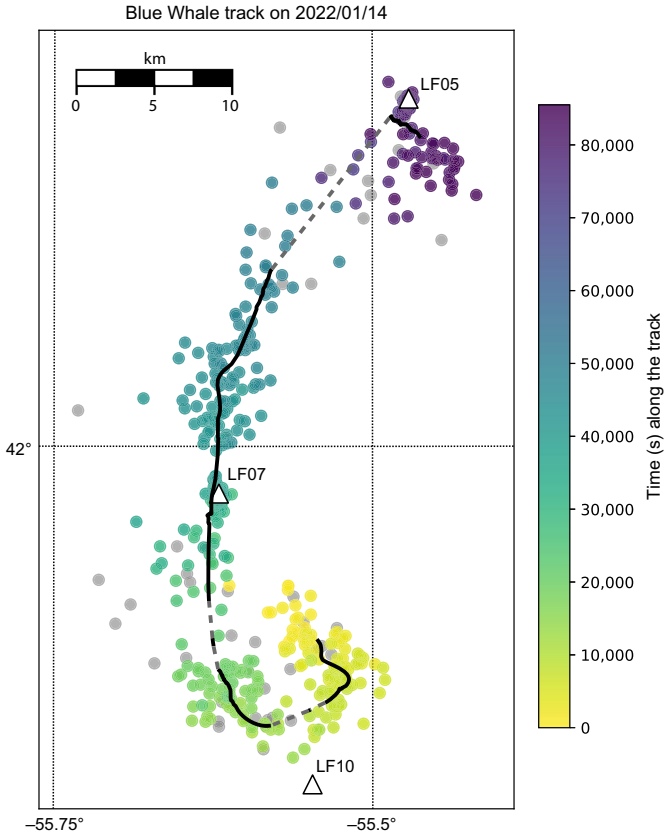


Figure 10. Daily track of a blue whale detected on 14 January 2022. The circles represent the final locations of individual whale calls, with the final 444 selected positions colored by time relative to the start of the day. The gray circles indicate detections that do not meet the cross-correlation selection criterion (fewer than two station pairs with CC ≥0.8), which are excluded from the smoothed track. The black line shows the moving average of the locations, with dashed segments highlighting spatial and temporal gaps in the track. The white triangles denote OBS stations. The color version of this figure is available only in the electronic edition.

with the call times highlighted for the 490 calls constrained by cross-correlation data. Even after cross-correlation-based relocations, considerable scatter remained in the positions of individual calls, so we created a smoothed track using a Gaussian-weighted moving window over 444 positions, yielding a representative track of the whale's average movement over 24 hr. The smoothed trajectory indicates a total travel distance of approximately 58 km if all calls are indeed from one whale, as we have assumed here. Although the track is composed of multiple songs separated by temporal (and corresponding spatial) gaps, a single continuous trajectory appears to reasonably fit the data.

Discussion and Conclusions

Given the variety of topics covered, we separate the discussion into four key areas before returning to an overall conclusion.

Downloaded from pubs.geoscienceworld.org/ssa/srl/article-pdf/doi/10.1785/0220260156/8340850/srl-2026156.1.pdf by Dalhousie Univ Libraries Serials/Killam Library user on 23 October 2026

1. Our ambient-noise cross-correlation workflow revealed that station LF02 accumulated a total clock drift of 1.14 s, whereas the other seven stations deviated by less than 0.08 s. Over the 87-day study period, LF02 drifted 13 ms per day, which is an order of magnitude higher than the manufacturer's drift specification for the Aquarius clock. However, no anomalous trends in internal temperature, humidity, or pressure were observed that could explain this behavior. The clock drift at station LF02 was corrected by incrementally adjusting the start time of each daily seismogram before subsequent analysis. Future deployments will ideally have a GPS clock synchronization for each OBS both before deployment and upon recovery, simplifying corrections, but this process can be applied in any situation where clock synchronization is not feasible.
2. PPSD and spectrogram analysis of OBS records revealed noise levels similar to many previous OBS deployments, including values that slightly exceed the NHNM in the 0.2–1 Hz microseism band. Above this frequency, noise levels gradually decrease up to ∼5 Hz, often necessitating application of a high-pass filter near this threshold for local earthquake analysis. Spectrograms revealed persistent features from natural phenomena such as the microseisms, internal tides, and whale calls, as well as minor features that may be related to the OBS stabilization under seafloor pressure and temperature conditions during the first few days after deployment. The ∼19° tilt computed for LF05 was unexpected but consistent with features observed in its PPSDs and teleseismic *P*-wave arrivals, suggesting that the estimate is robust. Its overall noise levels and SNR for teleseismic *P* waves (averaged across components) remained within expectations, suggesting good coupling with the seafloor, and there are no severe bathymetric features observed in the vicinity at the available resolution (Fig. 1). We propose that LF05 likely settled at a high tilt in very soft seafloor sediments.
3. The small catalog of 17 earthquakes provides the first depth estimates for earthquakes in the LFSZ, which reach up to ∼39 km relative to the seafloor, including a concentration of events at ∼30 km, about 20 km below the estimated Moho depth. Given that the oceanic lithosphere in this region is very old (∼150 Ma) and cold, brittle deformation extending far below the Moho into the uppermost mantle is not unexpected. However, OBS-based observations that directly resolve earthquake depths within oceanic lithosphere remain rare. Some estimated hypocenters are clearly too shallow (<1 km), including two (of 10) events that are within or reasonably near the OBS array. These likely reflect misinterpreted picks or instabilities associated with the very low-velocity surficial sediments. We also tested excluding the slowest, shallowest velocity layers, but this did not improve the stability of the solutions.

   We suggest that earthquakes in the LFSZ study area may be related to sediment loading due to the fan itself and the following isostatic adjustment, although loading may not be expected to produce such a highly linear zone without further structural controls. We further speculate that at some point in the tectonic history of the margin, transform motion could have diverted from the SW Grand Banks Transform to a transform that underlies the modern LFSZ, providing an alternative connection between the Cobequid–Chedabucto fault system and the Newfoundland transform zone and creating sizeable faults that are reactivated during present-day earthquakes. Although no offset in magnetic anomalies across the LFSZ is visible, the magnetic signature of the underlying igneous oceanic crust is largely obscured by the thick sediment sequence, so magnetic data does not preclude such a transform fault. We did not resolve earthquake focal mechanisms or stress in the LFSZ in this study. Future work may allow focal mechanisms to be determined for a subset of events using waveform-fitting approaches, although elevated noise levels at frequencies below ∼3 Hz may make it particularly challenging. If successful, focal mechanism and stress-orientation estimates could help support or rule out these proposed hypotheses.
4. This study reports what we believe is the first detection and localization of baleen whales in deep waters of the Northwest Atlantic, that is, away from the continental shelf, highlighting the value of OBS networks for (low-frequency) passive acoustic monitoring. We identified fin and blue whale calls, with fin whale INI ranging around 10–21 s, longer than the previously reported 10–15 s observed in shallower waters. Over the three-month dataset, we detected approximately 26,000 blue whale calls and 17,000 fin whale calls per OBS. As we have not associated all calls across stations, we do not have precise numbers of unique calls. This equates to over 20% of the recorded data containing blue whale songs, and ∼3% to 4% of the data containing fin whale songs. Both species are listed under Canada's Species at Risk Act, with the blue whale classified as endangered. Documenting their presence in deep offshore environments such as the Laurentian Fan provides important information on their range and critical habitat within Canadian waters. We also present an example blue whale track spanning an entire day, revealing an ∼58 km travel path across the OBS network. However, we find that it is difficult to resolve the precise positions of individual blue whale A–B calls, even when including cross-correlation data and azimuthal constraints.

This article summarizes the first long-term OBS deployment by the NFSI, which was also the first long-term, deep-water test of the Aquarius OBS model. Despite the dataset being shorter than intended and with fewer OBS, it provided an opportunity to assess their capacity to monitor earthquakes, baleen whales, and physical oceanographic phenomena. It also allowed us to assess the clock stability and noise characteristics of the OBS; however, because the OBS-equipped

Downloaded from pubs.geoscienceworld.org/ssa/srl/article-pdf/doi/10.1785/0220260156/8340850/srl-2026156.1.pdf by Dalhousie Univ Libraries Serials/Killam Library user on 23 October 2026

magnetometer and accelerometer were not recorded during this deployment, the instrument orientation and tilt inferred from these sensors should be validated against seismologically derived estimates in future deployments. Similarly, as this dataset lacks clock synchronization in the field, it would be interesting to compare the clock drift inferred from ambient-noise cross-correlation with the more direct measurement from GPS clock synchronization at deployment and upon recovery. There will be many opportunities for these tests given that, by September 2026, the NFSI will have deployed and recovered 11 additional OBS arrays since this initial experiment, in collaboration with various project partners and involving networks of up to 20–30 instruments.

Data and Resources

Laurentian Fan ocean-bottom seismometer data are archived at the National Facility for Seismological Investigations data center with the International Federation of Digital Seismograph Networks network code 17 (Nedimović *et al.*, 2021). Data processing and analysis were performed using Python, including open-source tools such as ObsPy and the OBStools package (https://github.com/nfsi-canada/OBStools, last accessed June 2026), specifically the ATACR module, for compliance and tilt-noise analysis. The supplemental material for this article includes Tables S1–S5 and Figures S1–S27.

Declaration of Competing Interests

The authors acknowledge that there are no conflicts of interest recorded.

Acknowledgments

The National Facility for Seismological Investigations (originally National Facility for Seismic Imaging; Nedimović, 2019) was created with funding from the Canadian Foundation for Innovation and matching funds from six provincial agencies. This included funds for a long-term facility testing that led to the Laurentian Fan deployment. The authors acknowledge support from the Natural Sciences and Engineering Research Council of Canada via Discovery Grants to Nedimović, Zhang, and Plourde, and via the iMAGE-CREATE program (Nedimović). The authors received further support from the Ocean Frontier Institute Seed Fund (Zhang). The authors thank the crews of the R/V Strait Explorer and R/V Coriolis II for their contributions. The authors thank Editor-in-Chief Allison Bent and Adam Ringler, as well as two anonymous reviewers, for their constructive comments that greatly improved this article.

References

Abbas, A., G. Zhu, J. Zi, H. Chen, and H. Yang (2023). Evaluating and correcting short-term clock drift in data from temporary seismic deployments, *Earthq. Res. Adv.* **3,** no. 2, 100199, doi: 10.1016/j.eqrea.2022.100199.

Adams, J., and P. Basham (1989). The seismicity and seismotectonics of Canada east of the Cordillera, *Geosci. Canada* **16,** no. 1, 3–16.

Audet, P., and H. Janiszewski (2020). nfsi-canada/OBStools: v0.1.0, *Zenodo*, doi: 10.5281/zenodo.4281480.

Audet, P., M. G. Bostock, D. C. Boyarko, M. R. Brudzinski, and R. M. Allen (2010). Slab morphology in the Cascadia fore arc and its relation to episodic tremor and slip, *J. Geophys. Res.* **115,** no. B4, doi: 10.1029/2008JB006053.

Bakun, W. H., and W. B. Joyner (1984). The M_L scale in central California, *Bull. Seismol. Soc. Am.* **74,** no. 5, 1827–1843, doi: 10.1785/BSSA0740051827.

Basham, P., and J. Adams (1983). Earthquakes on the continental margin of eastern Canada: Need future large events be confined to the locations of large historical events, *U.S. Geol. Surv. Open-File Rept. 83-843*, 456–467.

Bell, S. W., D. W. Forsyth, and Y. Ruan (2015). Removing noise from the vertical component records of ocean-bottom seismometers: Results from year one of the Cascadia Initiative, *Bull. Seismol. Soc. Am.* **105,** no. 1, 300–313, doi: 10.1785/0120140054.

Bensen, G. D., M. H. Ritzwoller, M. P. Barmin, A. L. Levshin, F. Lin, M. P. Moschetti, N. M. Shapiro, and Y. Yang (2007). Processing seismic ambient noise data to obtain reliable broad-band surface wave dispersion measurements, *Geophys. J. Int.* **169,** no. 3, 1239–1260, doi: 10.1111/j.1365-246X.2007.03374.x.

Bent, A. L. (1995). A complex double-couple source mechanism for the Ms 7.2 1929 Grand Banks earthquake, *Bull. Seismol. Soc. Am.* **85,** no. 4, 1003–1020.

Bent, A. L., and P. Voss (2022). Seismicity in the Labrador-Baffin Seaway and surrounding onshore regions, in *Geological synthesis of Baffin Island (Nunavut) and the Labrador-Baffin Seaway*, L. T. Dafoe and N. E. Bingham-Koslowski (Editors), Geological Survey of Canada, Ottawa, Ontario, Canada, Bulletin 608, 379–387.

Braunmiller, J., J. Nabelek, and A. Ghods (2020). Sensor orientation of Iranian broadband seismic stations from P-Wave particle motion, *Seismol. Res. Lett.* **91,** no. 3, 1660–1671, doi: 10.1785/0220200019.

Chang, E. T. Y., B. F. Chao, G.-Y. Chen, and J.-M. Liau (2016). Internal tides recorded at ocean bottom off the coast of southeast Taiwan, *J. Geophys. Res. Oceans* **121,** no. 5, 3381–3394, doi: 10.1002/2015JC011370.

Corela, C., A. Loureiro, J. L. Duarte, L. Matias, T. Rebelo, and T. Bartolomeu (2023). The effect of deep ocean currents on ocean-bottom seismometers records, *Nat. Hazards Earth Syst. Sci.* **23,** no. 4, 1433–1451, doi: 10.5194/nhess-23-1433-2023.

Courtney, R. C., and D. J. Piper (1992). The gravity signature of a large Quaternary depocentre off southeastern Canada, *Géogr. Phys. Quat.* **46,** no. 3, 349–360.

Crawford, W. C., and S. C. Webb (2000). Identifying and removing tilt noise from low-frequency (< 0.1 Hz) seafloor vertical seismic data, *Bull. Seismol. Soc. Am.* **90,** no. 4, 952–963, doi: 10.1785/0119990121.

Davis, G. E., M. F. Baumgartner, P. J. Corkeron, J. Bell, C. Berchok, J. M. Bonnell, J. Bort Thornton, S. Brault, G. A. Buchanan, D. M. Cholewiak, *et al.* (2020). Exploring movement patterns and changing distributions of baleen whales in the western North Atlantic using a decade of passive acoustic data, *Global Change Biol.* **26,** no. 9, 4812–4840, doi: 10.1111/gcb.15191.

Doxsee, W. (1948). The Grand Banks earthquake of November 18, 1929, *Publ. Dom. Obs. Ott.* **7,** 323–335.

Duennebier, F. K., and G. H. Sutton (1995). Fidelity of ocean bottom seismic observations, *Mar. Geophys. Res.* **17,** no. 6, 535–555, doi: 10.1007/BF01204343.

Downloaded from pubs.geoscienceworld.org/ssa/srl/article-pdf/doi/10.1785/0220260156/8340850/srl-2026156.1.pdf by Dalhousie Univ Libraries Serials/Killam Library user on 23 October 2026

Dunn, R. A., and O. Hernandez (2009). Tracking blue whales in the eastern tropical Pacific with an ocean-bottom seismometer and hydrophone array, *J. Acoust. Soc. Am.* **126,** no. 3, 1084–1094, doi: 10.1121/1.3158929.

Essing, D., V. Schlindwein, M. C. Schmidt-Aursch, C. Hadziioannou, and S. C. Stähler (2021). Characteristics of current—induced harmonic tremor signals in ocean—bottom seismometer records, *Seismol. Res. Lett.* **92,** no. 5, 3100–3112, doi: 10.1785/0220200397.

Ewing, J. I., and R. P. Meyer (1982). Rivera Ocean Seismic Experiment (ROSE) overview, *J. Geophys. Res. Solid Earth* **87,** no. B10, 8345–8357, doi: 10.1029/JB087iB10p08345.

Forsyth, D. W., and A. D. Chave (1994). Experiment investigates magma in the mantle beneath mid-ocean ridges, *Eos Trans. Am. Geophys. Union* **75,** no. 46, 537–540, doi: 10.1029/94EO02023.

Gaspà Rebull, O., J. D. Cusí, M. Ruiz Fernández, and J. G. Muset (2006). Tracking fin whale calls offshore the Galicia Margin, North East Atlantic Ocean, *J. Acoust. Soc. Am.* **120,** no. 4, 2077–2085, doi: 10.1121/1.2336751.

Gibb, R., E. Browning, P. Glover-Kapfer, and K. E. Jones (2019). Emerging opportunities and challenges for passive acoustics in ecological assessment and monitoring, *Methods Ecol. Evol.* **10,** no. 2, 169–185, doi: 10.1111/2041-210X.13101.

Godin, O. A., and D. M. F. Chapman (1999). Shear-speed gradients and ocean seismo-acoustic noise resonances, *J. Acoust. Soc. Am.* **106,** no. 5, 2367–2382, doi: 10.1121/1.428074.

Guo, H., and H. Zhang (2017). Development of double-pair double difference earthquake location algorithm for improving earthquake locations, *Geophys. J. Int.* **208,** no. 1, 333–348, doi: 10.1093/gji/ggw397.

Hable, S., K. Sigloch, E. Stutzmann, S. Kiselev, and G. Barruol (2019). Tomography of crust and lithosphere in the western Indian Ocean from noise cross-correlations of land and ocean bottom seismometers, *Geophys. J. Int.* **219,** no. 2, 924–944, doi: 10.1093/gji/ggz333.

Halchuk, S., T. I. Allen, G. C. Rogers, and J. Adams (2015). Seismic Hazard Earthquake Epicentre File (SHEEF2010) used in the fifth generation seismic hazard maps of Canada, *Geol. Surv. Canada Open-File 7724.*

Harmon, N., C. A. Rychert, J. M. Kendall, M. Agius, P. Bogiatzis, and S. Tharimena (2020). Evolution of the oceanic lithosphere in the equatorial Atlantic from Rayleigh wave tomography, evidence for small-scale convection from the PI-LAB experiment, *Geochem. Geophys. Geosys.* **21,** no. 9, e2020GC009174, doi: 10.1029/2020GC009174.

Harris, D., L. Matias, L. Thomas, J. Harwood, and W. H. Geissler (2013). Applying distance sampling to fin whale calls recorded by single seismic instruments in the northeast Atlantic, *J. Acoust. Soc. Am.* **134,** no. 5, 3522–3535, doi: 10.1121/1.4821207.

Hasegawa, H., and R. Hermann (1989). A comparison of the source mechanisms of the 1975 Laurentian Channel earthquake and the tsunamigenic 1929 Grand Banks event, in *Earthquakes at North-Atlantic Passive Margins: Neotectonics and Postglacial Rebound*, Springer, Dordrecht, Netherlands, 547–562.

Hasegawa, H., and H. Kanamori (1987). Source mechanism of the magnitude 7.2 Grand Banks earthquake of November 1929: Double couple or submarine landslide? *Bull. Seismol. Soc. Am.* **77,** no. 6, 1984–2004.

Hawley, W. B., R. M. Allen, and M. A. Richards (2016). Tomography reveals buoyant asthenosphere accumulating beneath the Juan de Fuca plate, *Science* **353,** no. 6306, 1406–1408, doi: 10.1126/science.aad8104.

Hutchinson, J., H. Kao, M. Riedel, K. Obana, K. Wang, S. Kodaira, T. Takahashi, and Y. Yamamoto (2023). Tectonic evolution of the Nootka fault zone and deformation of the shallow subducted Explorer plate in northern Cascadia as revealed by earthquake distributions and seismic tomography, *Sci. Rep.* **13,** 7873, doi: 10.1038/s41598-023-33310-z.

Hutchinson, J., H. Kao, G. Spence, K. Obana, K. Wang, and S. Kodaira (2019). Seismic characteristics of the Nootka fault zone: Results from the Seafloor Earthquake Array Japan–Canada Cascadia experiment (SeaJade), *Bull. Seismol. Soc. Am.* **109,** no. 6, 2252–2276, doi: 10.1785/0120190008.

Hyndman, R. D. (2015). Tectonics and structure of the Queen Charlotte fault zone, Haida Gwaii, and large thrust earthquakes, *Bull. Seismol. Soc. Am.* **105,** no. 2B, 1058–1075, doi: 10.1785/0120140181.

Janiszewski, H. A., Z. Eilon, J. B. Russell, B. Brunsvik, J. B. Gaherty, S. G. Mosher, W. B. Hawley, and S. Coats (2022). Broad-band ocean bottom seismometer noise properties, *Geophys. J. Int.* **233,** no. 1, 297–315, doi: 10.1093/gji/ggac450.

Kanazawa, T., M. Mochizuki, and H. Shiobara (2001). Broadband seismometer for a long-term observation on the sea floor, *Proc. of the OHP/ION Joint Symposium on Long-term Observations in the Oceans: Current Status and Perspectives for the Future*, S11–06 pp.

Kasahara, J., D. M. Hussong, and G. H. Sutton (1980). A seismic study using ocean-bottom seismometers near the Mid-Atlantic Ridge at 23° N, *Mar. Geol.* **35,** nos. 1/3, 199–218, doi: 10.1016/0025-3227(80)90031-6.

Keen, C., and R. Hyndman (1979). Geophysical review of the continental margins of eastern and western Canada, *Can. J. Earth Sci.* **16,** no. 3, 712–747, doi: 10.1139/e79-067.

Kolaj, M., J. Adams, and S. Halchuk (2020). The 6th generation seismic hazard model of Canada, *17th World Conf. on Earthquake Engineering*, Sendai, Japan, 13–18 September 2020.

Kolaj, M., S. Halchuk, and J. Adams (2023). Sixth-generation seismic hazard model of Canada: Final input files used to generate the 2020 National Building Code of Canada seismic hazard values (ver. 1.0), *Geol. Surv. Canada Open-File Rept. 8924.*

Lamontagne, M., and K. B. S. Burke (2018). The 1929 magnitude 7.2 Grand Banks earthquake: Felt reports from the dominions of Canada and Newfoundland and islands of Saint-Pierre and Miquelon, France, *Geol. Surv. Canada Open-File Rept. 8353.*

Lau, K. W. H., M. R. Nedimović, and K. E. Louden (2018). Continent-ocean transition across the northeastern Nova Scotian margin from a dense wide-angle seismic profile, *J. Geophys. Res. Solid Earth* **123,** no. 5, 4331–4359, doi: 10.1029/2017JB015282.

Linehan, D. (1940). Earthquakes in the West Indian region, *EOS Trans. AGU* **21,** no. 2, 229–232, doi: 10.1029/TR021i002p00229.

Liu, Y., A. Plourde, G. Cairns, K. Bosman, J. Thibodeau, E. Sirati, J. Chien, F. Darbyshire, M. Nedimović, M. Zhang, *et al.* (2026). Lower St. Lawrence Seaway Amphibious Seismic Network for earthquakes and marine soundscape monitoring, *Seismica* **5,** no. 1, doi: 10.26443/seismica.v5i1.2044.

Lomax, A., J. Virieux, P. Volant, and C. Berge-Thierry (2000). Probabilistic earthquake location in 3D and layered models: Introduction of a Metropolis-Gibbs method and comparison with

Downloaded from pubs.geoscienceworld.org/ssa/srl/article-pdf/doi/10.1785/0220260156/8340850/srl-2026156.1.pdf by Dalhousie Univ Libraries Serials/Killam Library user on 23 October 2026

linear locations, in *Advances in Seismic Event Location*, C. H. Thurber and N. Rabinowitz (Editors), Springer, Dordrecht, Netherlands, 101–134.

McGregor, B. A. (1979). Current meter observations on the US Atlantic continental slope—variation in time and space, *Mar. Geol.* **29,** nos. 1–4, 209–219, doi: 10.1016/0025-3227(79)90109-9.

McNamara, D. E., and R. P. Buland (2004). Ambient noise levels in the continental United States, *Bull. Seismol. Soc. Am.* **94,** no. 4, 1517–1527, doi: 10.1785/012003001.

Mellinger, D. K., and C. W. Clark (2003). Blue whale (Balaenoptera musculus) sounds from the North Atlantic, *J. Acoust. Soc. Am.* **114,** no. 2, 1108–1119, doi: 10.1121/1.1593066.

Mellinger, D. K., K. M. Stafford, S. E. Moore, R. P. Dziak, and H. Matsumoto (2007). An overview of fixed passive acoustic observation methods for cetaceans, *Oceanography* **20,** no. 4, 36–45, doi: 10.5670/oceanog.2007.03.

Morano, J. L., D. P. Salisbury, A. N. Rice, K. L. Conklin, K. L. Falk, and C. W. Clark (2012). Seasonal and geographical patterns of fin whale song in the western North Atlantic Ocean, *J. Acoust. Soc. Am.* **132,** no. 2, 1207–1212, doi: 10.1121/1.4730890.

Natural Resources Canada (1985). Canadian National Earthquake Database [Dataset], Canadian Hazards Information Service, doi: 10.17616/R3TD24.

Nedimović, M. R. (2019). Ocean bottom seismometer instrumentation in Canada, *CSEG Recorder*, **44,** no. 2, 12–17.

Nedimović, M., A. Plourde, M. Zhang, G. Cairns, K. Bosman, J. Thibodeau, V. Eville, T. Wilson, and L. Smith (2021). OBS test deployment on the Laurentian Fan [Data set], *International Federation of Digital Seismograph Networks*, available at https://www.fdsn.org/networks/detail/17_2021/ (last accessed September 2026).

Niksejel, A., and M. Zhang (2024). OBSTransformer: A deep-learning seismic phase picker for OBS data using automated labelling and transfer learning, *Geophys. J. Int.* **237,** no. 1, 485–505, doi: 10.1093/gji/ggae049.

Niu, F., and J. Li (2011). Component azimuths of the CEArray stations estimated from P-wave particle motion, *Earthq. Sci.* **24,** 3–13, doi: 10.1007/s11589-011-0764-8.

Normandeau, A., D. C. Campbell, D. J. Piper, and K. A. Jenner (2019). Are submarine landslides an underestimated hazard on the western North Atlantic passive margin? *Geology* **47,** no. 9, 848–852, doi: 10.1130/G46201.1.

Normandeau, A., D. J. Piper, J. Shaw, B. J. Todd, D. Calvin Campbell, and D. C. Mosher (2020). The seafloor of southeastern Canada, in *Landscapes and Landforms of Eastern Canada*, O. Slaymaker and N. Catto (Editors), Springer, Cham, Switzerland, 453–471.

Obana, K., M. Scherwath, Y. Yamamoto, S. Kodaira, K. Wang, G. Spence, M. Riedel, and H. Kao (2014). Earthquake activity in northern Cascadia subduction zone off Vancouver Island revealed by ocean-bottom seismograph observations, *Bull. Seismol. Soc. Am.* **105,** no. 1, 489–495, doi: 10.1785/0120140095.

Okal, E. A. (2008). The generation of T waves by earthquakes, *Adv. Geophys.* **49,** 1–65.

Pe-Piper, G., and D. J. Piper (2004). The effects of strike-slip motion along the Cobequid - Chedabucto - southwest Grand Banks fault system on the Cretaceous-Tertiary evolution of Atlantic Canada, *Can. J. Earth Sci.* **41,** no. 7, 799–808, doi: 10.1139/e04-022.

Peterson, J. R. (1993). Observations and modeling of seismic background noise, *U.S. Geol. Surv. Open-File Rept. 93-322*.

Pilkington, J. F., E. H. Stredulinsky, R. M. Abernethy, and J. K. Ford (2018). Patterns of fin whale (Balaenoptera physalus) seasonality and relative distribution in Canadian Pacific waters inferred from passive acoustic monitoring, *DFO Can. Sci. Advis. Sec. Res. Doc. 2018/032*.

Piper, D. J., D. A. Stow, and W. R. Normark (1983). The Laurentian fan: Sohm abyssal plain, *Geo-Mar. Lett.* **3,** no. 2, 141–146, doi: 10.1007/BF02462459.

Piper, D. J. W., P. Cochonat, and M. L. Morrison (1999). The sequence of events around the epicentre of the 1929 Grand Banks earthquake: Initiation of debris flows and turbidity current inferred from sidescan sonar, *Sedimentology* **46,** no. 1, 79–97, doi: 10.1046/j.1365-3091.1999.00204.x.

Piper, D. J. W., A. N. Shor, and J. E. Hughes Clarke (1988). The 1929 Grand Banks earthquake, slump, and turbidity current, in *Sedimentologic Consequences of Convulsive Geologic Events*, H. E. Clifton (Editor), Geological Society of America, Boulder, Colorado.

Plourde, A. P., and M. R. Nedimović (2021). Earthquake depths, focal mechanisms, and stress in the Lower St. Lawrence seismic zone, *Seismol. Res. Lett.* **92,** no. 4, 2562–2572, doi: 10.1785/0220200429.

Plourde, A. P., and M. R. Nedimović (2022). Monitoring fin and blue whales in the lower St. Lawrence Seaway with onshore seismometers, *Remote Sens. Ecol. Conserv.* **8,** 551–563, doi: 10.1002/rse2.261.

Poupinet, G., W. L. Ellsworth, and J. Fréchet (1984). Monitoring velocity variations in the crust using earthquake doublets: An application to the Calaveras fault, California, *J. Geophys. Res.* **89,** 5719–5731, doi: 10.1029/JB089iB07p05719.

Ramakrushana Reddy, T., P. Dewangan, L. Arya, P. Singha, and K. A. Kamesh Raju (2020). Tidal triggering of the harmonic noise in ocean-bottom seismometers, *Seismol. Res. Lett.* **91,** no. 2A, 803–813, doi: 10.1785/0220190080.

Roy, N., Y. Simard, F. Aulanier, and S. Giard (2018). Fin whale continuous frequentation of St. Lawrence habitats detected from multi-year passive acoustic monitoring (PAM), *DFO Canadian Science Advisory Secretariat Research Document 2018/059*.

Ruffman, A., and V. Hann (2006). The Newfoundland tsunami of November 18, 1929: An examination of the twenty-eight deaths of the "South Coast Disaster", *Nfld. Stud.* **21,** no. 1, 97–148.

Širović, A., A. Rice, E. Chou, J. A. Hildebrand, S. M. Wiggins, and M. A. Roch (2015). Seven years of blue and fin whale call abundance in the Southern California Bight, *Endang. Species Res.* **28,** 61–76, doi: 10.3354/esr00676.

Sousa-Lima, R. S., T. F. Norris, J. N. Oswald, and D. P. Fernandes (2013). A review and inventory of fixed autonomous recorders for passive acoustic monitoring of marine mammals, *Aquat. Mamm.* **39,** no. 1, 23–53, doi: 10.1578/AM.39.1.2013.23.

Stähler, S. C., M. C. Schmidt-Aursch, G. Hein, and R. Mars (2018). A self-noise model for the German DEPAS OBS pool, *Seismol. Res. Lett.* **89,** no. 5, 1838–1845, doi: 10.1785/0220180056.

Stanistreet, J. E., D. P. Nowacek, A. J. Read, S. Baumann-Pickering, H. B. Moors-Murphy, and S. M. Van Parijs (2016). Effects of duty-cycled passive acoustic recordings on detecting the presence of beaked whales in the northwest Atlantic, *J. Acoust. Soc. Am.* **140,** no. 1, EL31–EL37, doi: 10.1121/1.4955009.

Downloaded from pubs.geoscienceworld.org/ssa/srl/article-pdf/doi/10.1785/0220260156/8340850/srl-2026156.1.pdf by Dalhousie Univ Libraries Serials/Killam Library user on 23 October 2026

Stehly, L., M. Campillo, and N. M. Shapiro (2007). Traveltime measurements from noise correlation: stability and detection of instrumental time-shifts, *Geophys. J. Int.* **171,** no. 1, 223–230, doi: 10.1111/j.1365-246X.2007.03492.x.

Stow, D. A. V. (1981). Laurentian Fan: Morphology, sediments, processes, and growth pattern, *AAPG Bull.* **65,** no. 3, 375–393, doi: 10.1306/2F9197DD-16CE-11D7-8645000102C1865D.

Suetsugu, D., and H. Shiobara (2014). Broadband ocean-bottom seismology, *Annu. Rev. Earth Planet. Sci.* **42,** 27–43, doi: 10.1146/annurev-earth-060313-054818.

Sutton, G., F. Duennebier, B. Iwatake, J. Tuthill, B. Lewis, and J. Ewing (1981). An overview and general results of the Lopez Island OBS experiment, *Mar. Geophys. Res.* **5,** no. 1, 3–34, doi: 10.1007/BF00310309.

Todd, E. K., S. Y. Schwartz, K. Mochizuki, L. M. Wallace, A. F. Sheehan, S. C. Webb, C. A. Williams, J. Nakai, J. Yarce, B. Fry, *et al.* (2018). Earthquakes and tremor linked to seamount subduction during shallow slow slip at the Hikurangi Margin, New Zealand, *J. Geophys. Res. Solid Earth* **123,** no. 8, 6769–6783, doi: 10.1029/2018JB016136.

Tolstoy, I., and M. Ewing (1950). The T phase of shallow-focus earthquakes, *Bull. Seismol. Soc. Am.* **40,** no. 1, 25–51, doi: 10.1785/BSSA0400010025.

Toomey, D. R., R. M. Allen, A. H. Barclay, S. W. Bell, P. D. Bromirski, R. L. Carlson, X. Chen, J. A. Collins, R. P. Dziak, B. Evers, *et al.* (2014). The Cascadia Initiative: A sea change in seismological studies of subduction zones, *Oceanography* **27,** no. 2, 138–150, doi: 10.5670/oceanog.2014.49.

Toomey, D. R., S. C. Solomon, and G. M. Purdy (1988). Microearthquakes beneath Median Valley of Mid-Atlantic Ridge near 23°N: Tomography and tectonics, *J. Geophys. Res. Solid Earth* **93,** no. B8, 9093–9112, doi: 10.1029/JB093iB08p09093.

Trabattoni, A., G. Barruol, R. Dréo, and A. Boudraa (2023). Ship detection and tracking from single ocean-bottom seismic and hydroacoustic stations, *J. Acoust. Soc. Am.* **153,** no. 1, 260–273, doi: 10.1121/10.0016810.

Trehu, A. M. (1985). Coupling of ocean bottom seismometers to sediment: Results of tests with the U.S. Geological Survey ocean bottom seismometer, *Bull. Seismol. Soc. Am.* **75,** no. 1, 271–289, doi: 10.1785/BSSA0750010271.

Van Parijs, S. M., C. W. Clark, R. S. Sousa-Lima, S. E. Parks, S. Rankin, D. Risch, and I. C. Van Opzeeland (2009). Management and research applications of real-time and archival passive acoustic sensors over varying temporal and spatial scales, *Mar. Ecol. Prog. Ser.* **395,** 21–36, doi: 10.3354/meps08123.

VanDecar, J. C., and R. S. Crosson (1990). Determination of teleseismic relative arrival times using multi-channel cross-correlation and least-squares, *Bull. Seismol. Soc. Am.* **80,** 150–169.

Wadati, K., and S. Oki (1933). On the travel time of earthquake waves. (Part II), *J. Meteorol. Soc. Jpn. Ser. II* **11,** no. 1, 14–28, doi: 10.2151/jmsj1923.11.1_14.

Waldhauser, F., and W. L. Ellsworth (2000). A double-difference earthquake location algorithm: Method and application to the Northern Hayward Fault, California, *Bull. Seismol. Soc. Am.* **90,** no. 6, 1353–1368, doi: 10.1785/0120000006.

Waldhauser, F., and D. Schaff (2007). Regional and teleseismic double-difference earthquake relocation using waveform cross-correlation and global bulletin data, *J. Geophys. Res. Solid Earth* **112,** no. B12, doi: 10.1029/2007JB004938.

Walton, M. A., L. M. Staisch, T. Dura, J. K. Pearl, B. Sherrod, J. Gomberg, S. Engelhart, A. Tréhu, J. Watt, J. Perkins, *et al.* (2021). Toward an integrative geological and geophysical view of Cascadia subduction zone earthquakes, *Annu. Rev. Earth Planet. Sci.* **49,** 367–398, doi: 10.1146/annurev-earth-071620-065605.

Wamba, M. D., J.-P. Montagner, B. Romanowicz, and G. Barruol (2021). Multi-mode waveform tomography of the Indian Ocean upper and mid-mantle around the Réunion hotspot, *J. Geophys. Res. Solid Earth* **126,** no. 8, e2020JB021490, doi: 10.1029/2020JB021490.

Wang, Y., T. Yang, Y. Wu, D. Liu, X. Huang, J. Wang, W. Zhong, H. Shou, Y. Zhou, and Y. Chen (2022). A new broad-band ocean bottom seismograph and characteristics of the seismic ambient noise on the South China Sea seafloor based on its recordings, *Geophys. J. Int.* **230,** no. 1, 684–695, doi: 10.1093/gji/ggac092.

Webb, S. C. (1998). Broadband seismology and noise under the ocean, *Rev. Geophys.* **36,** no. 1, 105–142, doi: 10.1029/97RG02287.

Wilcock, W. S. D. (2012). Tracking fin whales in the northeast Pacific Ocean with a seafloor seismic network, *J. Acoust. Soc. Am.* **132,** no. 4, 2408–2419, doi: 10.1121/1.4747017.

Wingfield, J. E., B. Rubin, J. Xu, J. E. Stanistreet, and H. B. Moors-Murphy (2022). Annual, seasonal, and diel patterns in blue whale call occurrence off eastern Canada, *Endanger. Species Res.* **49,** 71–86, doi: 10.3354/esr01204.

Zhang, H., R. M. Nadeau, and M. N. Toksoz (2010). Locating nonvolcanic tremors beneath the San Andreas fault using a station-pair double-difference location method, *Geophys. Res. Lett.* **37,** no. 13, doi: 10.1029/2010GL043577.

Zhang, M., W. L. Ellsworth, and G. C. Beroza (2019). Rapid earthquake association and location, *Seismol. Res. Lett.* **90,** no. 6, 2276–2284, doi: 10.1785/0220190052.

Zhu, J., and L. Wen (2024). Hydroacoustic study of fin whales around the Southern Wake Island: Type, vocal behavior, and temporal evolution from 2010 to 2022, *J. Acoust. Soc. Am.* **155,** no. 5, 3037–3050, doi: 10.1121/10.0025776.

Manuscript received 10 April 2026
Published online 16 September 2026

Downloaded from pubs.geoscienceworld.org/ssa/srl/article-pdf/doi/10.1785/0220260156/8340850/srl-2026156.1.pdf by Dalhousie Univ Libraries Serials/Killam Library user on 23 October 2026